Journal of
ENERGY TECHNOLOGY

Journal of
ENERGY TECHNOLOGY

VOLUME 12 / Issue 4

JOURNAL OF ENERGY TECHNOLOGY

Spoštovani bralci revije Journal of energy technology (JET)

Ideja o soproizvodnji toplotne energije in električne energije je že dokaj stara. V primeru soproizvodnje se termodinamični in eksergijski izkoristek sistema močno izboljšata. Prva delujoča elektrarna s tipom soproizvodnje električne in toplotne energije je bila termoelektrarna na premog Pearl Street Station (Manhattan v New Yorku, ZDA), zgrajena leta 1882. Pri gradnji je sodelovalo podjetje Edison Illuminating Company, ki je bilo v lasti poznanega izumitelja Thomasa Edisona. Toplotno energijo oz. paro je elektrarna dovajala lokalnim proizvajalcem, hkrati so se okoliški prebivalci že takrat ogrevali s toplotno energijo. Teorija in praksa uporabe soproizvodnje toplotne in električne energije sta se ves ta čas nadgrajevali in izboljševali. Danes sodobne elektrarne s soproizvodnjo električne in toplotne energije delujejo tako z jedrskim gorivom in premogom kot ostalimi gorivi. Z naraščanjem potreb po uporabi obnovljivih virov energije so se začele razvijati tudi tehnike soproizvodnje toplotne in električne energije s pomočjo sončne energije. Eden takšnih primerov je predstavljen tudi v tej številki, kjer je prikazana uporaba fotovoltaike za soproizvodnjo.

Jurij AVSEC
odgovorni urednik revije JET

Dear Readers of the Journal of Energy Technology (JET)

The concept of the cogeneration of electricity and heat is quite old. The thermodynamic and exergy efficiency of cogeneration systems is much improved. The first coal cogeneration power plant was the Coal Pearl Street Station, which started operating in Manhattan, New York in 1882. The thermal power plant was built with the help of the Edison Illuminating Company, owned by the famous inventor Thomas Edison. The power plant supplied heat or steam to local producers, while the residents of the area were heating with thermal energy. The theory and practice of the use of cogeneration have continued to be improved and improved. Today, modern power plants with cogeneration work with both nuclear fuel, coal, and other fuels. With the increasing demand for renewable energy, techniques for cogeneration of heat and electricity with the help of solar energy have begun to develop. This issue presents one such example, which illustrates the use of photovoltaics for cogeneration.

Jurij AVSEC
Editor-in-chief of JET

Table of Contents /
Kazalo

Journal of Energy Technology

THE EXTERNAL BIAS-DEPENDENT ELECTRIC FIELD AT HOLE-INJECTING ELECTRODE/α-NPD JUNCTION AND ITS RELATIONSHIP TO GAUSSIAN DISORDERED INTERFACE STATES

OD ZUNANJE NAPETOSTI ODVISNO ELEKTRIČNO POLJE OB STIKU VRZELI VBRIZGAJOČE ELEKTRODE/α-NPD IN POVEZAVA Z NEUREJENIMI ENERGIJSKIMI STANJI VMESNE PLASTI

Bruno Cvikl [℞]

Keywords: electrode/organic electric field, contact affected hole mobility, organic interface disorder parameters

Abstract

An alternative interpretation of two different sets of published temperature-dependent current-voltage α-NPD (i.e. N,N´-Di(1-naphthyl)-N,N´-diphenyl-(1,1´-biphenyl)-4,4´-diamine) organic semiconductor data is presented. The measurements are described in terms of the hole drift current density expressed with two parameters: the electric field at the hole-injecting interface, E_{int}, and, μ_{max}, the hole mobility determined by the measured current density at the maximum value of the externally applied electric field, E_a, in a given experiment. The former parameter, depending on the contact résistance, may be a function of E_a but the latter is E_a independent, The fixed value of E_{int} signifies the occurrence of the space charge limited current, SCLC, within the electrode/α-NPD structures

[℞] Corresponding author: Professor Emeritus Bruno Cvikl, PhD., University of Maribor, Maribor, Slovenia and Jožef Stefan Institute, Ljubljana, Slovenia, E-mail address: bruno.cvikl@ijs.si

and the contact is ohmic. Then, the calculated weak bias-dependent hole drift mobility, a function of Eint, equals the well-known exponential bias-dependent mobility, and saturates. The data not displaying SCLC characteristics are used for the calculation of Eint dependence on the applied field, Ea. It is shown that the quasi-ohmic contacts cause Eint to become a strong double-valued function of the externally applied electric field, Ea, described in terms of the distorted, inverted, high order parabola. The corresponding bias-dependent hole drift mobility is non-exponential and evolves on a considerably lower level than in SCLC cases. It is found that a sufficiently increased Ea alters the quasi-ohmic contact/α-NPD region into the ohmic one. A simple model of a thin, net hole charged, electrode/α-NPD interface enables the relationship between the deduced interfacial electric field, Eint, and the Ea dependent Gaussian width, σ, as well as the energy shift of its peak, φ, along the negative binding energy is to be investigated. The current-voltage method appears to be a helpful expedient for the investigation of the electric field at hole-injecting electrode/organic interfaces.

Povzetek

Članek podaja alternativno fizikalno interpretacijo dveh primerov v literaturi objavljenih temperaturno odvisnih meritev gostote toka v odvisnosti od pritisnjene napetosti na vzorcih α-NPD (i. e. N,N´-Di(1-naftil)-N,N´-difenil-(1,1´-bifenil)-4,4´-diamin) organskega polprevodnika. Meritve gostote toka vrzeli so v pričujočem članku popisane z dvema parametroma: z jakostjo električnega polja, Eint, na vmesni plasti elektroda/organski polprevodnik kjer se vrzeli vbrizgavajo v organski medij in, μmax, mobilnost vrzeli, ki je določena z izmerjeno gostota toka pri maksimalni vrednosti zunanje električne poljske jakosti, Ea, danega eksperimenta. Parameter, Eint, ki je funkcija kontaktne napetosti, lahko zavisi še od Ea, toda drugi parameter je od Ea neodvisna konstanta. Nespremenjena vrednost Eint z vrednostjo Ea podaja obstoj t. im. omejenega toka zaradi prostorskega naboja, SCLC, v vzorcu α-NPD s čimer je tedaj električni kontakt opredeljen kot ohmski stik. V tem primeru je izračunana, šibko Ea, odvisna mobilnost vrzeli podana z dobro poznano eksponentno odvisnostjo, ki vodi do nasičenja mobilnosti vrzeli. Eksperimentalni podatki, ki ne zadoščajo merilom SCLC so uporabljeni za izračun odvisnosti Eint od zunanjega polja Ea. Izkaže se, da zaradi kvazi-ohmskega kontakta postane Eint dvolična funkcija zunanjega pritisnjenega polja Ea, ki zavzame obliko skrivljene in invertirane parabole višjega reda. Temu ustrezna mobilnost vrzeli se izraža v ne-eksponentni formi is zavzame vrednosti, ki so bistveno pod nivojem vrednosti izračunane v primerih opredeljenih z SCLC značilnostmi. V delu je pokazano, da je mogoče z dovolj velikim zunanjim poljem, Ea, preoblikovati kvazi-ohmski kontakt v ohmskega. Poenostavljeni model tenke, z vrzeli nasičene, vmesne plasti elektroda/α-NPD omogoča proučevanje vzajemnega odnosa med električnim poljem vmesne plasti Eint in od Ea odvisno širino Gaussove funkcije razmazanosti energijskih stanj vrzeli v organskem polprevodniku in pa energijski pomik le-te vzdolž negativne vezavne energije. Eksperimentalna metoda gostota toka - napetost se izkaže, kot nadvse ustrezna metoda za raziskave električne poljske jakosti z vbrizganimi vrzeli odlikovane vmesne plasti stika elektrode/organski polprevodnik.

1   INTRODUCTION

All organic semiconductor electrical devices are developed with the aim that the resistance between the injecting (and ejecting) charges from the suitable electrode into the organic is minimized. Improvements in the resistance of the electrode/organic semiconductor contact result in considerably improved device performances on account of advances of the charge carrier mobility. The science of so-called contact engineering [1-7] crucially contributes to the optimized performance of the distinct organic devices that are in use. The charge mobility μ is an involved function of the externally applied electric field, E_a, the temperature T, and the charge carrier density, ρ, providing that the injection barrier between the charge-injecting electrode and the contacting organic semiconductor is as small as possible. The charge mobility is most commonly inferred by the current-voltage, $j – V_a$, experiments in which the stead- state current density, j, through the electrode/organic/metal structures as a function of the externally applied DC electric field, $E_a = V_a/L$, is measured. Here V_a is the applied voltage over the two electrodes and L is the thickness of the organic medium between them. The prerequisite for its successful determination is the existence of ohmic contacts between the charge injecting electrode/organic interfaces. The current through such a structure is then the space charge limited current, SCLC, and only under this condition the data then provide the fully reliable charge-carrier mobility [3, 8, 9]. The criteria for the occurrence of SCLC are based on the effects of the electric field-dependent charge mobility, organic layer thickness and charge-injection barrier height as extensively discussed by Wang et. al. [8, 9]. It was concluded that these condition should be fulfilled prior to the measurements; otherwise the obtained results apparently "have no meaning" [9]. In cases of non-ohmic contacts the current density no longer exhibits the SCLC behavior. A thorough investigation into the reproducibility problem of the mobility measurements in organic semiconductors that concludes with the recommendations regarding the device preparation, fabrication, measurement and analyses in order to ensure the most trustworthy results has been reported recently by Blakesley et al. [10].

The above-stated works and others that have followed provide evidence that under identical conditions the hole mobility of a given organic substance is a function of the electrode material utilized for injection of holes. Evidently, the cause that influences the hole mobility ought to be related to the electric field at the hole-injecting interface. This expectation is explicitly expressed in the form of the steady-state non-zero electric field at the charge-injecting electrode/organic interface, E_{int}, that is a parameter in the extended Mott-Gurney space charge limited current model [11]. The second parameter of the stated law is the maximum value of the charge mobility, μ_{max}, (in [11] inappropriately termed effective mobility μ_{eff} as will be discussed later) that is in a given current-voltage experiment determined from the current density measured (exclusively) at the maximum value of E_a. The parameter μ_{max} is consequently bias independent. It should be stressed that both parameters are related to the charge drift mobility, μ_d, which is the quantity of great practical interest. As shown in [11], the SCLC fits in various organic samples based on the extended Mott-Gurney law are characterized by the external bias independent, parameter E_{int}, see for instance Fig. 1 and Fig. 2 of [11]. In cases of poor ohmic contacts the current density is no longer of the SCLC type, which commonly occurs (at least) within the initial part of the interval of the externally applied electric field $E_a \geq 0.1$ MV/m say, see Figs. 3, and 4 of [11]. The SCLC is in the extended Mott-Gurney formulation described in terms of a non-zero constant E_{int}, which is independent of the externally applied electric field, E_a. This was empirically verified by the independent SCLC analyses based upon the well-known Mott-Gurney expression incorporating

the exponential bias dependent mobility [11]. As seen, there the SCLC predictions of Eqs. (1), and (2) considerably overshoot the j-V data within the initial part of the respective Ea interval. In contrast to this, it was found that in cases of a non-ohmic metal/organic contact, the concave SCLC curve formulated by the extended Mott-Gurney model can always be made to intersect (at least) the first and the last current-voltage measuring point of a giving Ea interval.

Recently, a particularly interesting current-voltage temperature and thickness dependent hole transport measurements within the various electrode/α-NPD (i.e., N,N´-Di(1-naphthyl)-N,N´-diphenyl-(1,!´-biphenyl)-4,4´-diamine) organic thin diode devices have been published by Rohloff et al. [12] and van Mensfoort et al. [13]. In [13] it was determined that Mott-Gurney law with the exponential bias-dependent mobility could not account for their data. Consequently, the given set of current density measurements, [13], on a ITO/α-NPD/Pd hole only organic structure, offers the information related to the current density deviation from the expected SCLC behavior. In contrast to this, for the hole only PEDOT:PSS/α-NPD/ TCTA/MoO3/Al organic structures the occurrence of SCLC has been determined by j-V measurements as reported by Rohloff et al. [12]. Here PEDOT:PSS denotes poly(3,4-ethylenedioxythiophene):polystyrene sulfonate and TCTA is an abridged notation for tris(4-carbazoyl-9-ylphenyl)amine. It is evident that in case of the stated organic structures prepared with chemically identical organic semiconductor α-NPD that the observed difference in the hole current density (between the samples of equal thickness and at similar temperature) should be related to the different hole injecting electrodes. The data of [12], and [13] then provide an opportunity to arrive at some additional information of not-yet understood processes that occur at the hole-injecting electrodes/α-NPD interfaces. In this respect, the investigation of the electric field at the hole-injecting electrodes/α-NPD interface, Eint, a parameter of the extended Mott-Gurney law [11], seems to be most convenient.

This is the purpose of the presented work. Namely, as written above, Eint is in an organic structure related to the charge drift mobility, μd and no detail knowledge exists in the literature about its relationship to the non-SCLC current density, j. The later process occurs due to the non-ideal electrode/organic contact. The explicit knowledge of Eint dependence on the externally applied field Ea (note that in SCLC cases Eint, is a constant, [11]) should then provide additional illumination of the charge transport processes and by this on the expected performance of a given organic structure. It will be shown that the current density deviation from the SCLC behavior in α-NPD hole transporting electrode/organic structures occurs on account of the external bias dependence of the electric fields, Eint, at hole injecting contacts, which detrimentally affects the hole drift mobility.

It is known, and [12] and [13] offer support to the claim that the interface between the electrode and the organic substance plays a crucial role in the charge transfer between the stated two media. It primarily depends on the relative alignment of molecular energy states in the organic to the Fermi level of the electrode giving rise to the energy barrier at the interface.

On account of a low density of free charge within the organic bulk, the electric field applied between the two electrodes results in a charge imbalance at the organic side of the charge injecting interface. The imbalance may be particularly large if the electrical contacts are ideal ohmic. The SCLC, the space charge limited current through the metal/organic/metal structure at a given applied electric field, Ea, is determined by the ability of the charge injecting electrode to continuously supply excess charges to the interface in the amount exceeding the steady current through the organic that is limited by space charge in its interior [14, 15]. On account of the interaction between the adsorbed organic molecules and the electrode the additional energy

states develop at the contact that depend on the method of the organic deposition, the organic crystallinity, and on number of other possible factors, The complex array of resultant energy barriers on the interface represents a cause that a portion of injected charges, the ones with insufficient energies accumulate (become trapped) in it. The free excess charge supplied by the contact the net trapped holes on those parts of α-NPD molecules that constitute the interface the charge on the organic side of the interface that compensate the built-in voltage, the charge at the electrode/organic contact and other possible sources of charge all contribute to the resultant electric field within the α-NPD organic.

The electrode/organic interface charging, i.e. the charge transient processes, before the steady state current is established is most suitable investigated by the time-resolved electric-field-induced optical second-harmonic generation, EFISHG, method [16, 17]. With the stated technique the electric fields in organic layers can be selectively and directly probed [16, 17]. In comparison to the EFISHG method it will be shown that the current-voltage method is suitable for the investigation of the steady state electric field at the charge injecting interface. It will be shown that the electric field at the hole injecting interface, Eint, as used in this paper represents the magnitude of the resulting vector $\vec{E}int = \vec{E}_a + \vec{E}_{ch}$ at the position of the interface. Here Ech stands for the magnitude of the (steady state) electric field due to all other, unspecified, sources of charge and Ea, is the externally applied (steady state) electric field over the device.

It is noted that the authors of [12] and [13] have successfully interpreted their measurements in terms of the drift-diffusion theory of the hole mobility subjected to the charge hopping among the energy states described by the static, uniform, Gaussian energetic disorder in α-NPD organic bulk [18]. Assuming the hopping hole transport within the Gaussian distribution of disordered energy levels in the organic the authors have shown that the Gaussian disorder model (GDM) [19], reproduces the measurements well. This model takes into account the hole mobility described as a known function of the hole density, the electric field, the temperature, and the Gaussian width, σ. Likewise, it was shown that the correlated Gaussian disorder model (CDM) [20] also accounts for the data well. The CDM model contains additional description of the site energy correlated disorder due to the randomly oriented dipoles and may be viewed as an upgrade of the GDM description. No direct interaction between the hole-injecting electrodes and the α-NPD organic has been considered.

In [21] the charge transfer from the electrode into the density of states within the organic bulk has been considered and suggested that the spread of the disordered energy states near the interface appeared to be correlated with the charge mobility. This important question is presently also addressed and the relationship between the bias-dependent Eint (the principle cause of affecting the hole drift mobility) and the disordered energy states within the organic part of the interface is established on the basis of a simple interface model constructed upon the findings of Oehzelt et al., [22].

This paper is organized as follows:

In Sec. 2, a brief presentation of the extended Mott-Gurney law is given and the method of Eint extraction is presented. It is shown that the original Mott-Gurney law describing SCLC is valid for Eint = c Ea, where c is an electrode/organic specific constant. A simple model is presented by which the compatibility of the deduced results with Gaussian energetic disorder in organic is established. In Sec. 3.1, the predictions of the hole drift current density, j, are compared to the published current-voltage data of [12]. It is shown that the forward biased (i.e. Al at the positive

potential) PEDOT:PSS/α-NPD(100 nm)/TCTA(5 nm)/MoO3/Al structure displays SCLC characteristics only for Ea exceeding a given temperature-dependent threshold value within the respective Ea interval of measurements. Within the SCLC region, characterized by the constant Eint, the calculated Ea dependence of the hole drift mobility, μ_d, coincides with the prediction of the well-known exponential dependent hole mobility. This is the region of good ohmic contact. The small current density deviation from the SCLC characteristic is used to calculate the Ea dependence of Eint, and to investigate its effect on the hole drift mobility. Based upon the simple model the relationship between the deduced Eint and the hole transport within the Gaussian distribution of disordered energy states within the organic side of the interface is demonstrated and characterized. In Section 3.2 the absence of SCLC characteristics for all temperature-dependent current-voltage measurements on the ITO/α-NPD/Pd organic structure of [13] is determined. The strong bias dependence of Eint is evaluated and the detrimental effect of its Ea dependence on the drift hole mobility is demonstrated. In Sec. 4 the conclusions drawn are presented.

On the basis of the results presented here the current/voltage method might be of interest also in the area of contact engineering.

2   THE EFFECT OF THE ELECTRODE/ORGANIC CONTACT ON CURRENT-VOLTAGE DATA

It was shown in [11] that the extended Mott-Gurney law describes the steady state current density within the single layer metal/organic structure that originates due to the externally applied DC electric field, Ea, and reflects the complicated electrode/organic processes, which directly govern the charge transport. These processes have generally been neglected in the analyses of current-voltage measurements from which the charge mobility is most often extracted.

Throughout this work, the hole-injecting electrode at the positive potential, Va, is considered at the origin of the frame of reference and the cathode is placed at the position x = L, where L is the thickness of the organic layer. The general expression of the hole drift current density is then expressed by the extended Gurney-Mott law, [11], that explicitly considers the charge-injecting interface of a given metal/organic structure and reads,

$$J \; = \; \varepsilon\varepsilon_0\mu_d\frac{E_a^2}{L} \tag{2.1}$$

where, j is the (steady state) current density, ε, is the relative permittivity of the organic layer, $\varepsilon 0$ is the permittivity of vacuum, Ea = Va/L, is the externally applied DC electric field over the organic structure and μ_d is Ea dependent charge carrier drift mobility, defined as,

$$\mu_d \; = \; \frac{\mu_{max}}{2}$$

$$\left\{\frac{9}{8} - \frac{3}{2}\left(\frac{E_{int}}{E_a}\right)^2 + \left[\frac{81}{64} - \frac{3}{4}\left(\frac{E_{int}}{E_a}\right)^4 + 3\left(\frac{E_{int}}{E_a}\right)^3 - \frac{27}{8}\left(\frac{E_{int}}{E_a}\right)^2\right]^{\frac{1}{2}}\right\} \quad (2.2)$$

The charge drift mobility, μd, depends on the organic morphology, intrinsic and extrinsic impurities, method of deposition, strengths of the charge-phonon interactions that determine the charge drift transport among the disordered energy states of the organic bulk, etc.

The stated model is characterized by two distinct, independent physical parameters; (a) the nonzero electric field at the charge injecting electrode/organic interface, Eint, [11] that is in this work investigated as a function of the externally applied electric field, Ea, and (b) the maximum value of the charge mobility μmax as measured in a given experiment..Evidently, in the (forbidden limit) Eint = 0, see [11], Eq. (2.1) would have reduced into the original Mott-Gurney law, [14]. It is characterized by the charge density singularity, [14] at the charge-injecting interface. By postulating the existence of the non-zero electric field at the charge-injecting electrode/organic interface, Eint ≠ 0, this deficiency is remedied, [11]. It can be noted, however, that for the ratio Eint/Ea = c, where c is a given constant 0 < c < 1 the charge drift mobility Eq. (2.2) is Ea independent. Simple rearrangements of terms then result in the expression,

$$j = \frac{9}{8}\,\varepsilon\,\varepsilon_0\,\mu\,\frac{V_a^2}{L^3} \quad (2.3)$$

where the so called effective charge mobility, μ, [14], identified as 8 μd/9, is bias Va independent. Eq. (2.3) represents the original version of Mott-Gurney law that describes the SCLC condition of the drift current density within the given organic semiconductor. As seen, Eq. (2.3) is in fact valid when the non-zero ratio Eint/Ea is a given constant, i.e. Eint ≠ 0, and represents a particular example of Eq. (2.1).

However, it has been realized that the charge mobility, μ, Eq. (2.3) is in fact on the externally applied electric field, Ea, dependent parameter, [23]. With the current-voltage measurements of large number of organic semiconductors it was empirically determined that μ may be suitably formulated in terms of the phenomenological exponential bias-dependent charge mobility given by,

$$\mu = \mu_0\,e^{\beta\sqrt{E_a}} \quad (2.4)$$

The last two expressions taken together traditionally describe the SCLC (i.e. the maximum steady current density that a given electrode/organic structure may sustain) and are very often used in current-voltage experiments for experimental determination of the charge mobility, [8-10]. It was shown, [11] that the general expression for hole current density j, Eq. (2.1), leads to SCLC only under the condition that Eint is Ea independent quantity in which case the contact is defined as ohmic. The deviation of the given current density from the shape of SCLC curve is then reflected in a bias dependence of Eint (remember that μmax is fixed since it is for a given organic structure extracted from the maximal value of the current density, jmax, as obtained at maximum Ea). The bias dependence of Eint is determined in two steps. Initially, the (fixed) parameters EintSCLC, and μmax, are determined so that the trial SCLC fit, Eq. (2.1), intersects the first and the last current

density points of the given Ea interval of measurements. With µmax known the bias dependence of Eint is then described by the (positive) roots of Eq. (1) evaluated successively for each experimentally determined pair (j, Ea). Note that the first and the last current density points are measured at two different values of Ea. Both points are characterized by identical value of Eint = EintSCLC, Consequently, Eint is a double valued function of the parameter Ea in all cases in which the current density defies the SCLC description.

The relationship exist among the electric field at the charge-injecting electrode/organic interface, Eint, the externally applied electric field, Ea, and the electric field at the site of the interface due all other charges present within the organic, Ech. It is deduced by observing that the resultant electric field within the organic layer is, $\vec{E} = \vec{E}a + \vec{E}ch$ see [16]. Written explicitly for the (thin) charged electrode/organic interface placed at the coordinate origin x = 0 the spatial dependent internal electric field, E(x), is then equal to

$$E(x) \equiv \left[E_{int}^2 \ + \ 2 \ \frac{j(E_a)}{\varepsilon \, \varepsilon_0 \, \mu_{max}} \ x \right]^{1/2} \ = \ E_a \ + \ E_{ch}(x)$$

(2.5)

Note that the interfacial electric field, Eint, is incorporated within the left term. Consequently, Ech(x) then represents the resultant electric field within organic due to all other sources except Eint. Since the hole-injecting interface is at the position x = 0, it immediately follows that,

$$E_{int} = E_a \ + \ E_{ch}$$

(2.6)

where Ech(x = 0) = Ech. Consequently, current-voltage experiments directly provide the interfacial electric field, Eint, see Eq. (2.1), and with Eq. (2.6) its relation to the electric field at the site of the interface that results from the distribution of other charges existing within the organic is presented.

The compatibility of the current-voltage data analyses using the above-presented method with the notion of the charge transport within the Gaussian disordered energy states in the organic is illustrated by virtue of a simple model described below.

Lange et al. [21], have reported that the band bending in organics may be explained by the transfer of charge from the electrode into the tail of Gaussian distribution of energy states, DOS, which extends into the organic charge transport gap. The space charge formed by occupation of tail states strongly modulates the width of Gaussian energetic disorder at the electrode-organic contact and in such a way appears to affect the charge mobility. Since, as shown presently, the bias dependence of the hole drift mobility is greatly influenced by the electric field at the hole-injecting electrode/α-NPD interface it remains to show that the hole drift mobility (or equivalently the electric field Eint) and the Gaussian energetic disorder at the electrode/α-NPD contact are mutually interrelated. To show this, a simple physical model is constructed. It is assumed that the interface may be represented as a plane sheet of uniformly distributed holes that occupy the disordered energy states at the organic side of the contact. Specifically, Oehzelt et al. [22], have determined that in thermal equilibrium in absence of the externally applied electric field, Ea = 0, the nonzero charge density is spontaneously induced at the metal/organic contact. This fact triggers a shift of the central position of the Gaussian energetic disorder in the direction of the increased (negative) binding energy [22]. The prediction has been verified by Whitcher et al. [24, 25], and Khoshkho et al. [26]. More specifically, Beck et al., [27], have with

the infrared spectroscopy method determined (at Ea = 0) that the charge at the Mo3/CBP interface where CBP denotes (4,4´-bis(N-carbazolyl)-1,1´-biphenyl) organic semiconductor decays to a very small value already within about 3 nm into the CPB organic bulk.

 With an extension of the ideas of [22] to cases in which the externally applied electric field is non-zero, Ea ≠ 0, it was already possible: (a) to show that the room temperature linearly increasing electric field at the hole-injecting ITO/P3HT (i.e. poly(3-hexylthiopene)) interface leads to the negative field hole mobility, [28], and (b) to provide the evidence of the relationship between the linearly dependent interfacial electric field and the Gaussian energetic disorder, σ, within the narrow region of the P3HT organics close to the hole-injecting metal/organic interfaces [28].

In order to investigate the relationship between the Ea dependent electric field at the hole-injecting electrode/organic interface and the Gaussian energetic disorder in the organic a simple model has been constructed, [28]. Considering the interface as a thin, laterally infinite, uniformly charged plane (in presence of steady electric fields) than from the Gauss law $\varepsilon\varepsilon_0 \oint \vec{E}_{int} d\vec{S}$ = $q(p_t + p_f)$ it follows that Eint = γint/($2\varepsilon\varepsilon_0$). Here pt, and pf are the (number) densities of trapped and free charge on the interface and γint denotes the interface charge density per unit area. In parallel to [28] and elaborating the approach of [22] and [27], it is now assumed that L* nm thick, laterally unlimited, organic layer in contact with an electrode is covered by an excess hole (areal) density that is in the first approximation equal to q ρ L* P(E) = 2 ε ε0 Eint, where P(E) is the probability that the disordered interfacial energy states are populated. The width L* chosen in this work, is the distance from the electrode/organic contact into the organic bulk at which the induced interface charge density is reduced to a small value, see Fig. 2a of [22], and Fig. 2 of [27]. The holes within the layer represent the seat of the interfacial electric field, Eint. The holes populate the disordered energy states within the organic interface, which are described in terms of Gaussian distribution function characterized by its width, σ, and the energy shift, φ. The stated relationship then reads,

$$E_{int} \quad = \quad \frac{q\,\rho\,L^*}{2\,\epsilon\,\epsilon_0\,\sigma\,\sqrt{2\pi}} \int_{-\infty}^{\infty} \frac{\exp[-\frac{1}{2}\left(\frac{E-E_H+\varphi}{\sigma}\right)^2]}{1+\exp[\frac{-E+E_F}{k\,T}]} \, dE \qquad (2.7)$$

where EH is the highest occupied molecular orbital (HOMO), and EF is the Fermi level. In this work the energy shift, φ, and the width of the Gaussian, σ, are assumed to be implicit functions of the externally applied electric field, Ea. Evidently, the stated two parameters are fixed for constant Eint (SCLC conditions) but in case of the external bias-dependent Eint their bias dependence should vary in a particularly coordinated way on account that Eint is then a double-valued function of Ea. It is noted that Eq. (2.7) is: (a) independent of the hole mobility, and (b) that the product q ρ L*, the interface (areal) hole charge density plays the role of the scaling factor only. For reference the number of charged molecules per unit area the (saturation) value of ρ L* = 8×1013 cm-2 is in [27] deduced from the measurements.

3   RESULTS AND DISCUSSION

3.1   The PEDOT: PSS/α-NPD(100 nm)/TCTA(5 nm)/MoO3/Al current-voltage data of Ref. [12]

The room temperature j-V measurements of the PEDOT:PSS/α-NPD(100 nm)/MoO3/Al organic structure of [12] were reported to exhibit unexpected behavior. The work functions of PEDOT:PSS is 5.1 eV, the HOMO level of the amorphous α-NPD is at 5.4 eV (i.e., the hole barrier between the two is then 0.3 eV) and the work function of MoO3 is placed at 6.86 eV, [12]. Contrary to the expectations it was found that the hole current density in the reverse direction (Pedot:PSS contact at the positive potential) exceeds the hole current in forward direction of bias, i.e., when the Al contact is at a positive potential. The authors report, [12] that the current density symmetry in the forward and backward direction of current is established by the deposition of 5 nm thick tris(4-carbazoyl-9-alphenyl)amine (TCTA) interlayer between the α-NPD and the MoO3/Al electrode.

The stated current density asymmetry effect will now be tentatively explained. In the reverse direction of bias, the barrier at PEDOT:PSS/α-NPD junctions appears to be small enough for the hole SCLC to take effect. However, the Al contact at the positive potential results in an unexpectedly weak current density, an effect that may be explained by the finding of Matsushima et al., [29]; in their study of the effect of the molybdenum trioxide layer placed between the ITO and α-NPD organic on the hole current transport the authors of [29] provide evidence that, under the stated polarity, the α-NPD/MoO3 interface becomes charged. Specifically, it is claimed that α-NPD boundary layer of the interface is charged positively while the MoO3 one negatively. Such a charged layer then detrimentally affects the hole injection from the MoO3/Al electrode. It is a fact that with the 5 nm thick TCTA layer between the α-NPD organic and the positively biased MoO3/Al electrode, [12], the SCLC regime is activated in the stated organic structure. This observation evidently supports the conjecture of Matsushima et al., [29], that in the forward direction of bias the α-NPD/MoO3 interface becomes charged. If this is indeed so, it may be clarified by the time-resolved electric-field-induced optical second-harmonic generation, EFISHG, investigation in combination with the steady current voltage measurements of the type as reported recently by Nishi et al. [16].

The forward hole current (positive potential at Al) within the PEDOT:PSS/α-NPD(100 nm)/TCTA(5 nm)/MoO3/Al organic structure was reported to be of the SCLC type, [12]. Then it is expected that from calculated curve with the bias-independent electric field, Eint, Eq. (2.1), at the hole-injecting TCTA/ α-NPD interface, should describe the data well. Consequently, the room temperature T = 295 K measurements, [12], are compared to the SCLC fit predicted by Eq. (2.1) (solid triangles) that connects the first and the last data point of the L = 100 nm thick sample (solid hexagons). In all calculations reported here the relative dielectric constant ε = 3. The parameters of this initial (trial) SCLC fit are found to be: the maximum hole mobility is μ_{max} = 3.7×10-8 m2/Vs and the interfacial electric field is Eint = 1.5 MV/m, see Fig. 1. As seen in Fig. 1 an excellent fit to the T = 295 K data of [12] is indeed obtained but only within the range say, Ea ≥ 1.0×107 V/m, Fig. 1. Thus, within the interval 10.0 MV/m ≤   Ea ≤ 25.0 MV/m the electric field at the hole-injecting interface (Eint = 1.5 MV/m), is constant and the bias dependence of the current density, j, is governed by the product μ_d Ea2. The hole drift mobility μ_d is weakly bias-dependent within the stated interval, as will be shown later. The fact that a clear disagreement between the SCLC fit and the data is observed within the interval of the applied electric field, 0.194×107 V/m ≤ Ea

≤ 1.0×107 V/m, Fig. 1, signifies that the Al/MoO3/TCTA/5 nm)/α-NPD(100 nm)/PEDOT:PSS organic structure (Al at the positive bias Va) is not barrier-free within the stated Ea interval.

For the Al electrode (at the origin of the frame of reference) at positive bias, Va > 0 then follows that within the interval 1.94 MV/m ≤ Ea ≤ 25.0 MV/m the interfacial field Eint < Ea, see Fig 2. This fact demonstrates that the (organic side of) the hole-injecting interface is exposed to an additional (steady) electric field in the opposite direction of Ea. This electric field due to the space charge and other charge sources (Eint is excluded) is denoted as Ech. In fact, it will be observed that the relationship Eint < Ea, is valid for all cases reported here even for non-SCLC current density conditions. Consequently, for the particular structure under investigation TCTA/α-NPD is identified as the hole-injecting interface, and it is feasible that the space charge and perhaps also the α-NPD/PEDOT:PSS interface represent a positively charged source of the (steady-state) interfacial electric field, Ech, acting in the opposite direction to Ea. The stated organic structure represents then a particular example of an organic bilayer, [16]. The resulting steady-state electric field at the hole-injecting interface TCTA/α-NPD is equal to Eint = Ea - Ech, see Eq. (6), in agreement with the experimental fact that Eint < Ea. The Eint represents the electric field at the TCTA/α-NPD contact that is directed towards the cathode in the positive direction of the x-axis.

The stated difference between the trial SCLC fit and the data within 1.94 MV/m ≤ Ea ≤ 10.0 MV/m interval will now be analyzed. As seen, Fig. 1, the initial current density point jinit = 15.75 A/m2 at Ea = 1.94 MV/m and likewise j = 1079.35 A/m2 at Ea = 10. 0 MV/m, are both characterized by already deduced SCLC parameters Eint = 1.5 MV/m, and μ_{max} = 3.7×10-8 m2/Vs. Following the procedure described in Sec. 2 the bias-dependent interfacial electric field, Eint, within the stated Ea interval is evaluated and the resulting electric field at the hole-injecting interface, Eint, is exhibited on Fig 2 (circles). Within the stated narrow Ea interval, it attains the shape of the distorted, inverted high order parabola that is analytically described by the approximation function presented in Table 1. It is noted that Eint is double-valued function of the argument Ea. The parameters of the SCLC curve well describing the data for Ea ≥ 10 MV/m are shown in Table 2. Inserting the deduced bias-dependent Eint and the maximum hole mobility, μ_{max} back into Eq. (2.1), the newly calculated fit practically coincides (as it should) with the data throughout the remaining part of the measuring interval (the crosses over the measuring points, i.e., solid hexagons), Fig. 1.
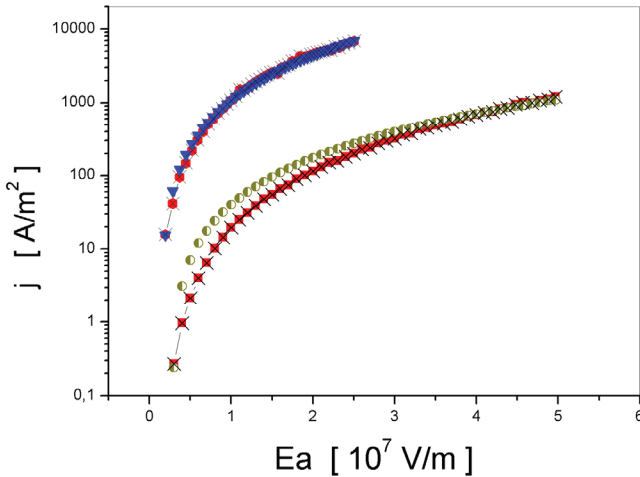
Figure 1: *Top curves: the comparison of the calculated trial SCLC curve (filled triangles) to the PEDOT:PSS/α-NPD(100 nm)/TCTA(5 nm)/MoO$_3$/Al hole j - E$_a$ data of [12] measured at T = 295 K (filled hexagons) reveals the existence of SCLC regime at values of the externally applied electric field E$_a \geq$ 10 MV/m. Bottom curves: the calculated trial SCLC curve (half-filled circles) to the data at T = 213 K (filled squares) of [12] exhibits the narrow SCLC regime only for E$_a \geq$ 41.8 MV/m. Crosses joined by the thin curve that in both examples coincide with the measurements denote the predictions of Eq. (2.1), when incorporating the deduced and for each temperature appropriate E$_a$ dependent electric field at the hole-injecting α-NPD(100 nm)/TCTA interface, E$_{int}$, see Fig. 2.The data are redrawn from Fig. 2b of Ref. [12].*

Viewing the T = 295 K curve (Fig. 1) the slow continuous merger of the SCLC fit to measurements that is taking place within the certain narrow range of Ea is noted. Consequently, Fig. 1 provides evidence that the quasi-ohmic contact may transit into a good ohmic one by an appropriate increase of the externally applied electric field, Ea. It is, however, unclear if this process is reversible. At this point, it should be stated that as seen in Fig. 1 the transition occurs continuously and it is not feasible that this interval could be univocally determined. For this reason such an interval is in this work replaced by a single current density point (here defined at Ea = 10.0 MV/m) at which both curves still coincide. This simplification affects the obtained results in two ways: (a) the calculated values of Eint are progressively scattered with increasing Ea, and (b) the derivative of the function Eint = Eint(Ea) with respect the argument Ea is then discontinuous at the point of merger, see Fig. 2. It should be emphasized that the magnitude of the T = 295 K resulting (bias-dependent) interfacial electric field, Eint, within the initial part of the Ea interval, i.e., within the quasi-ohmic region, 1.94 MV/m $\geq$ Ea $\geq$ 10 M2.V/m, considerably exceeds the one that characterizes the SCLC regime (i.e., Eint = 1.5 MV/m), see Fig. 2 (circles).
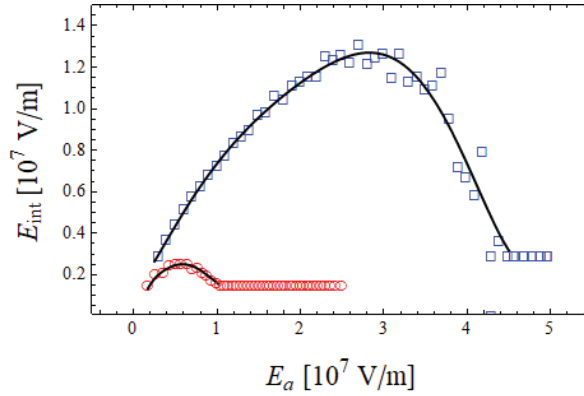
Figure 2: *The calculated electric fields at the hole-injecting electrode/α-NPD(100 nm) interface, E_{int}, as a function of the applied electric field, E_a, are exhibited for cases of the hole j - E_a data of [12]. The deduced interfacial electric field at T = 295 K (circles) and T = 213 K (squares) are represented by the approximation functions given in Table 1, and are shown by thin curves in Fig. 2. The constant E_{int}, characterize the E_a regions of SCLC regime indicating the ohmic resistance at the hole-injecting contact.*

Inserting the two parameters μ_{max} = 3.7×10-8 m2/(Vs), and Eint = 1.5 MV/m into Eq. (2), the calculated bias-dependent SCLC hole drift mobility, μ_d, at T = 295 K is exhibited in Fig. 3 (stars). For comparison with Eq. (2.3) the predicted fit with the exponential bias-dependent mobility, Eq. (2.4), (empty squares) is also included in Fig. 3. The parameters of the stated mobility are found to be: μ_0 = 3.6×10-8 m2/(Vs), and β = 0.4×10-4 (m/V)1/2. As shown in Fig. 3 the evaluated mobility, μ, Eq. (2.4), and μ_d, Eq. (2.2) considerably differ within the initial part of the Ea interval. The calculated curves within SCLC region practically coincide, a behavior similar to the one reported; see Fig. 4 of [11]. However, the correct bias dependence of the hole drift mobility is obtained only when Eq. (2.2) is calculated with the bias-dependent Eint; see Fig. 2 (circles). The result is exhibited in Fig. 3 (solid points) and the strong Ea dependence of μ_d, at small values of the externally applied electric field, Fig. 3, within the range of disagreement between the data and the (trial) SCLC curve is evident. The calculated curve is characterized by the relatively slower increase of the hole drift mobility with Ea (solid points) occurring entirely within the quasi-ohmic region, Fig. 3. Consequently even at T = 295 K the sample of [12] was not absolutely barrier-free. Over Ea > 10 MV/m the ohmic region is attained that is characterized by the constant value of Eint = 1.5 MV/m. This is the region within which the hole drift mobility, Eq. (2.2), exhibits very weak Ea dependence as evidenced on Fig. 3. The bias-dependent exponential hole drift mobility, Eq. (2.4), is at Ea = 25.0 MV/m then equal to μ_d = 4.4×10-8 m2/(Vs). The stated interval represents the saturation region of the electric field at the hole-injecting electrode/organic interface. Consequently, the SCLC region is the region within which the parameter, Eint, the interfacial electric field is independent of the externally applied electric field, Ea. Then the hole drift mobility, Eq. (2.2), is itself only weakly Ea dependent and for this reason the current density, Eq. (2.1), within the saturation region is almost proportional to Ea2.

Table 1: *Approximation functions for the temperature dependent electric field at the hole injecting TCTA/α-NPD organic interface of the form $E_{int} = a + b\,E_a + c\,E_a^2 + d\,E_a^3 + e\,E_a^4 + f\,E_a^5 + g\,E_a^6$ are shown. E_a denotes the externally applied electric field.*

T [K]	a [V/s]	b	c [(V/s)$^{-1}$]	d [(V/s)$^{-2}$]	e [(V/s)$^{-3}$]	f [(V/s)$^{-4}$]	g [(V/s)$^{-5}$]
PEDOT:PSS/α-NPD(100 nm)/TCTA/MoO$_3$/Al Ref. [12]
213	-1.039×10^6	1.733	-1.826×10^{-7}	1.392×10^{-14}	-5.750×10^{-22}	1.172×10^{-29}	-9.450×10^{-38}
295	-1.232×10^6	2.618	-9.311×10^{-7}	2.009×10^{-12}	-2.469×10^{-20}	1.527×10^{-27}	-3.693×10^{-35}
ITO/α-NPD(100 nm)/Pd Ref. [13]
189	-1.872×10^7	4.287	-2.354×10^{-7}	8.897×10^{-15}	-1.814×10^{-22}	1.939×10^{-39}	-8.607×10^{-39}
295	2.815×10^8	-88.586	1.136×10^{-5}	7.349×10^{-13}	2.564×10^{-20}	-4.609×10^{-28}	3.348×10^{-36}

Table 2: *The temperature dependent maximum hole mobility, μ_{max}, of the electrode/α-NPD(100 nm) thick organic entity and the associated electric field at the hole-injecting interface, E_{int}, are presented. Both quantities, based on published measurements of Rohloff et al., [12], and van Mensfoort et al., [13], are deduced by Eq. (2.3) at the maximum value of the externally applied electric field, E_a^{max}.*

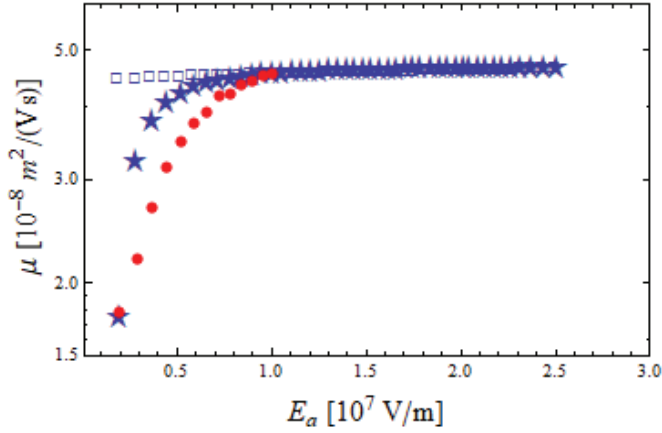| T [K]	μ_{max} [10^{-8} m^2(Vs)$^{-1}$]	E_{int} [10^7 Vm^{-1}]	E_a^{max} [10^7 Vm^{-1}]	Ref.
\multicolumn{4}{c}{PEDOT:PSS/α-NPD(100 nm)/TCTA/MoO$_3$/Al}	*[12]*
213	**0.15**	**0.29**	**5.0**	
295	**3.7**	**0.15**	**2.5**	
\multicolumn{4}{c}{ITO/α-NPD(100 nm)/Pd}	*[13]*
189	**0.013**	**2.20**	**7.5**	
295	**0.08**	**1.41**	**3.1**	

Figure 3: *The E_a dependence of the room temperature hole drift mobility within the α-NPD structure of [12] is shown. Assuming the SCLC regime to exist within the entire interval of measurements then: (a) the exponential bias-dependent hole mobility, Eq. (2.3), with the parameters, $\mu_0 = 3.6\times10^{-8}$ m²/(Vs), and $\beta = 4.0\times10^{-5}$ (m/V)$^{1/2}$ is described by empty squares, and (b) the hole drift mobility, μ_d, calculated from Eq. (2.2) with the constants $E_{int} = 1.5$ MV/m, and $\mu_{max} = 3.7\times10^{-8}$ m²/(Vs) is shown by stars. The μ_d curve denoted by solid points represents the predictions (within the non-SCLC region) of Eq. (2.2) evaluated with bias-dependent E_{int} of Fig. 2 (circles). Within the SCLC interval of bias, all three curves coincide.*

At this point it has to be emphasized that μmax depends on the coordinate (Eamax, j(Eamax)) of the measured current-voltage end point. Consequently, μmax is evidently Eamax sensitive, and so are the deduced bias-dependent Eint values. The initial, i.e., the first current density point with coordinates (Eamin, j(Eamin)) defines the initial intersection with the calculated (trial) SCLC curve and, consequently, this point is primarily related to the value of the second SCLC parameter, the bias-independent interfacial electric field, Eint. Discarding some given number of measurements within the highest range of the Ea interval (i.e. narrowing the given Ea interval) then the value of μmax, the maximum hole mobility is decreased and, consequently, the set of bias-dependent interfacial fields calculated within the narrow Ea interval (relative to the narrowed SCLC curve) is also correspondingly changed. However, the bias-dependent hole drift mobility curves, Eq. (2,2), calculated for each data set separately are found to coincide (within the shorter Ea interval) and thus prove that the magnitude as well as the bias-dependence of the hole drift mobility, μd, is invariant to the width of the Ea interval. Thus, the auxiliary parameters the bias-independent μmax and the bias-dependent set of evaluated Eint then via Eq. (2.2) define the bias-dependent hole drift mobility as a unique material property of the electrode/organic entity under the investigation.
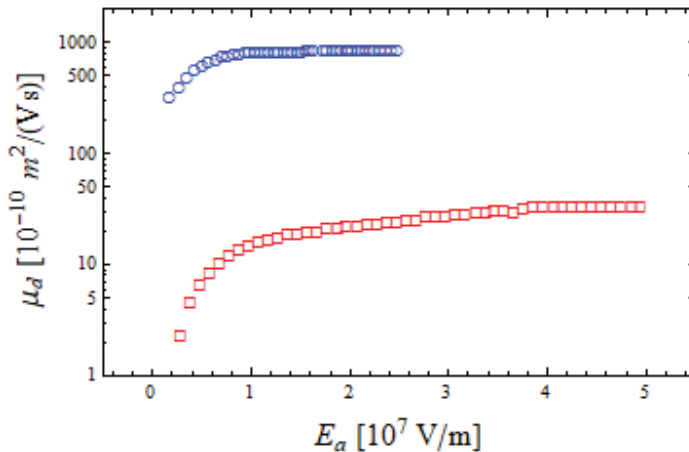
Figure 4: *The E_a dependence of the calculated hole drift mobility, μ_d, Eq. (2.2) incorporating the deduced bias dependence of E_{int} at T = 295 K (circles) and T = 213 K (squares), within the α-NPD(100 nm) structure of [12] is shown The growing part of the curves denote the quasi-ohmic contact region that with the increasing E_a continuously evolves into the ohmic region of (almost) the constant values of μ_d (compare Fig. 2).*

The results of the similar analyses as above of the data measured at T = 213 K, [12], are also shown on Fig. 1 (filled squares). It is immediately evident that the initial (Eint = 2.9 MV/m and μmax = 1.5×10-9 m2/Vs) SCLC fit calculated from Eq. (1) (half filled circles) exhibits within the interval (e.g. 3.0 MV/m $\leq$ Ea $\leq$ 41.8 MV/m) a noted disagreement to the data set. However, beyond that, i.e., within 41.8 MV/m $\leq$ Ea $\leq$ 50 MV/m interval the agreement between this initial (trial) SCLC curve and the measurements is evident. It is noted that the calculated SCLC curve using the above two bias-independent parameters again intersects the first and the last current-density data point. This is then a clear indication that the SCLC regime within the given structure (at the stated temperature) occurs within the highest range of the Ea interval only. Thus it is confirmed that the ohmic region of the PEDOT:PSS/α-NPD(100 nm)/TCTA(5 nm)/ MoO3/Al structure is temperature dependent and may be induced by the external bias, Ea. The ohmic region at T = 213 K has considerably narrowed in comparison to the one at T = 295 K. In addition the measuring Ea interval has substantially widened. Following the previously described steps, the bias-dependent interfacial electric field, Eint, is calculated, and together with the approximation function, Table 1, is exhibited in Fig. 2 (squares). Within the interval 41.8 MV/m $\geq$ Ea $\geq$ 45.0 MV/m the calculated values of Eint are considerably scattered. This occurs due to the fluctuations in reading off the (finite sized) data points that almost coincide with the SCLC fit, see Fig. 1. However, when the calculated bias-dependent Eint is inserted into Eq. (2.2), then the fit, Eq. (2.1) to the measured data is once again excellent (represented by the thin line passing through the crosses), Fig. 1. Once again it is observed that the magnitude of bias-dependent Eint considerably exceeds the corresponding (but bias-independent) value within the (narrow) SCLC region, Fig. 2. The Ea dependence of the hole drift mobility, Eq. (2.2), at T = 213 K is presented in Fig. 4, (empty squares).

Thus far, the emphasis has been on the dependence of the electric fields, Eint, at hole-injecting TCTA/α-NPD interfaces, as a function of the externally applied electric field, Ea, and an excellent agreement with the published data has been obtained. Quite similar quality fits are presented in

[12], and [13], but their calculations were based on the drift-diffusion hole transport using the well known models of the hole mobility characterized by hopping between the disordered energy states of the organic bulk as described by the Gaussian distribution function [18 - 20]. In particular, their results have shown that the half widths, σ, of the Gaussian disordered states, depending on the particular case investigated, should be placed within the interval 0.08 eV $\leq \sigma \leq$ 0.14 eV. It is noted that σ is independent of the applied electric field and describes an average over the organic sample.

The essential difference between the results reported in the literature and the findings presented here is the fact that at all temperatures the (temperature dependent) electric field at the hole-injecting TCTA/α-NPD interface is non-zero and definitely non-exponential. In addition, the resulting findings are obtained devoid of any phenomenological parameters. It is interesting that the data of [12], and [13], are in the present work also interpreted to an excellent approximation but seemingly on wholly unrelated basis. Consequently, it appears that the Gaussian disorder model and this work might be somehow related. The cause that different studies of hole mobility performed under similar conditions on chemically identical α-NPD organic semiconductor provide rather inconsistent results (compare for instance Figs. 4 and 8) is, in this work, attributed to unequal conditions at the hole-injecting interfaces, see Fig. 2, and Fig. 8.

In [21] the charge transfer from the electrode into the density of states within the organic bulk has been identified and it was suggested that the spread of the disordered energy states near the interface appeared to be correlated with the charge mobility. Consequently, it now remains to show that the above derived bias-dependent electric field at the hole-injecting TCTA/α-NPD interface, Eint = Eint(Ea), is related to the Gaussian energetic disorder at the organic side of the interface in conjunction with findings described in [18 - 20].

The deduced Eint, the inverted and distorted high order parabolas, are (for non-ohmic contacts) all double valued functions of the argument Ea, see Fig. 7. The calculations based on Eq. (2.7) are performed in the reverse order starting with Eint at the maximum value of the applied field, Ea, and proceed in a step-wise fashion towards its initial value. With the decreasing Ea, the corresponding value of the (bias-dependent) interfacial electric field, Eint, increases, attains its relative maximum and then decreases, as seen in Fig. 7. In the calculations the following parameters were used: ρ = 1.4×1027 m-3, see [13], L* = 5 nm, ε = 3, EH = 5.4 eV, EF = 5.1 eV, [12]. The thickness L* = 5 nm of the hole charged interface is chosen such that the (areal number) density ρL* of charged molecule is comparable with the similar value quoted in [27]. However, since this factor is just a scaling factor its exact magnitude is not crucial for the discussion that follows.

In the analyses of the lowest temperature T = 213 K data reported, [12], taking into consideration Eint shown on Fig. 2 (filled squares), the value for σ was set to σ = 0.11 eV (squares), (Eint = 2.9 MV/m at Eamax = 50.0 MV/m) and the energy shift was then found φ = 0.7197 eV (crossed circles). The bias dependence of the pair (σ, φ) exhibits shapes similar to the ones above and are shown in Fig 5. Despite the particular precaution taken by authors of [12] to eliminate the potential barrier at the hole-injecting TCTA/α-NPD interface, the barrier is nevertheless still present within the interval 2 MV/m < Ea < 42.0 MV/m as evidenced by the bias dependent interfacial electric field, Fig. 2.

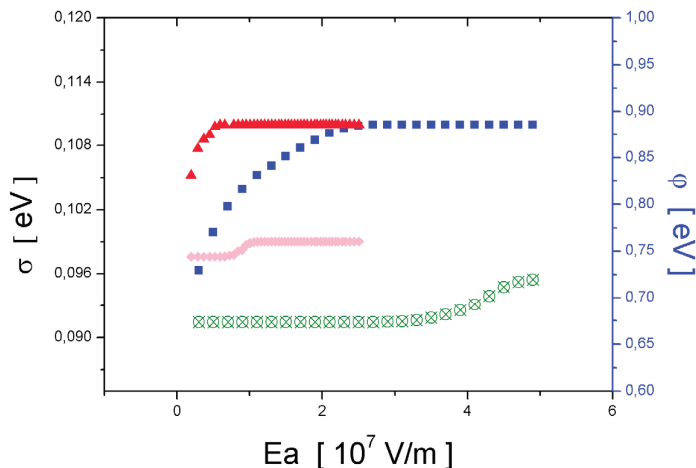**F*igure* 5**: *The E_a dependence of the Gaussian width, σ, (left scale) calculated from Eq. (2.7) for the values of E_{int} that are shown on Fig. 2: T = 213 K (filled squares), and T = 295 (filled triangles) is exhibited. The E_a dependence of the energy shift, φ, (right scale) of Gaussian peak is presented for T = 213 K (crossed circles) and T = 295 K (diamonds).*

As seen, the interfacial electric field deduced from T = 295 data of [12] is bias-dependent within the initial interval 2 MV/m $\leq$ Ea $\leq$ 10 MV/m, see Fig. 2 (circles), while above it the SCLC regime prevails and Eint attains a constant value Eint = 1.5 MV/m (squares). The constant value of Eint is according to Eq. (2.7) reflected in bias-independent pair (σ, φ) and Eint then indicates the existence of a stationary, bias-independent, small potential barrier against the injection of holes at the respective interface.

A comment about the nature of the double valued inverted parabolas Eint with the increasing Ea is now in order. The increasing part of the Eint curve is related to the diminishing value of σ keeping the constant value of φ, while the decreasing part of Eint illustrates the increasing energy shift φ, at the constant value of the Gaussian width, σ. Consequently, in this way the meaning of the apparent double valued Eint with the increasing Ea is clarified.

In this section, a relationship of Eint with the Gaussian disorder energy states at the interface is thus established. It is well-known that the GDM model, [18], describes the charge hopping transport within the Gaussian disordered states in organics that is characterized by the constant width. It is demonstrated above that at given temperature the bias-independent interfacial electric field, Eint, is related not only to the bias-independent Gaussian width but also to the bias-independent energy shift of its peak. Such a specific case occurs only under the SCLC condition characterized by the (relative) highest attainable values of the hole drift mobility, μd, that then exhibit a weak monotonic increase with the externally applied electric field, see Fig. 3. As presented here, none of the samples investigated in [12] and [13] has been truly barrier-free within the investigated Ea interval of measurements.

3.2 The ITO/α-NPD(100 nm)/Pd current-voltage data of Ref. [13]

Taguchi et al., [17], have investigated the room temperature IZO/α-NPD(200 nm)/Al organic structure by EFISHG method, in which IZO is the indium zinc oxide. Independently of the polarity of bias, it was determined that the electric field within the α-NPD organic is directed from anode to cathode (as expected) with the electrodes being charged accordingly. No other phenomena have been reported. This observation is here interpreted as the evidence that the so-called build-in voltage between the anode and cathode is compensated by a suitable collection of charge on the appropriate interface. The evidence that such compensation of the built-in voltage is also taking place in bilayer organic structures has been provided by Nishi et al., [16].

Van Mensfoort et al., [13] have reported the j – V results of the temperature and thickness dependent hole transport measurements in the amorphous small-molecule organic semiconductor α-NPD. The diode structures of the type ITO/α-NPD(L)/Pd, the organic thicknesses being L=100 nm and 200 nm are described in [13] in terms of the well-known charge transport models. The ITO contact was assigned as the anode.

In the previous section, it was shown that the fit to the SCLC data enables the two parameters, Eint, as well as μmax of Eq. (2.2) to be simultaneously deduced. It is observed that the current density data at low Ea are weakly displaced from the SCLC curve. Using the previously determined μmax, such data then enable the bias dependence of Eint to be determined from Eq. (2.1). However, in examples of strong deviation of data from the SCLC characteristics, the bias-independent parameter μmax ought to be evaluated separately. This is accomplished by using the trial SCLC curve that intersects the first and the last current density point within the appropriate interval of Ea. The procedure is illustrated as follows.

The data of [13] are again tested for the SCLC regime characterized by the two bias-independent parameters: Eint, and μmax. The disagreement between the data and the (trial) SCLC curve represents a measure of the contact deficiency. According to [11] and as shown above, the maximum hole mobility, μmax, is determined from the fit of Eq. (2.1) through the current density point at the maximum Ea, within its respective interval while in the first approximation is Eint represented by the initial, but slightly decreased value of Ea. In the next step, Eint is refined so that the calculated, postulated SCLC current density curve also intersects the first current-density data point at the initial value of the Ea interval. The experimental data of [13] and the calculated, Ea dependent, trial SCLC current density curves intersecting the data at corresponding abscissa values Eamin and Eamax are shown in Fig. 6 for L = 100 nm sample of [13]. The SCLC parameters for the room temperature T = 295 K measurements are Eint = 14.1 MV/m, and μmax = 7.5×10-10 m2/Vs determined within 14.12 MV/m $\leq$ Ea $\leq$ 31.4 MV/m (experiment – solid diamonds, calculations – solid triangles). At the lowest temperature T = 189 K the corresponding (trial) SCLC values obtained are Eint = 21.96 MV/m, and μmax = 1.3×10-10 m2/Vs within 22.0 MV/m $\leq$ Ea $\leq$ 74.9 MV/m (experimental data – filled squares, calculations – tiny diamonds), see Fig. 6.
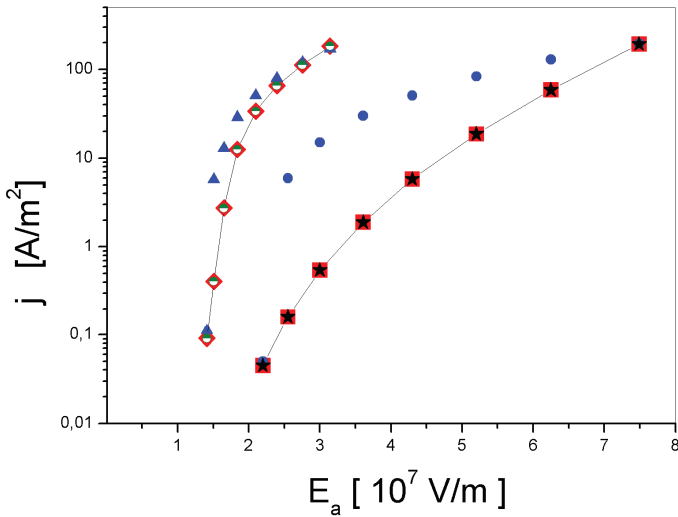
Figure 6: *The ITO/α-NPD(100 nm)/Pd hole j - E_a data measured at T = 295 K (diamonds) and at T = 189 K (squares) of [13] are compared to the calculated trial SCLC curves (triangles at T = 295 K, and tiny diamonds at T = 189 K). It is shown that by using the relevant temperature deduced bias dependent electric field, E_{int}, see Fig. 7, at ITO/α-NPD interface then by Eq. (2.1) calculated fits (T= 295 K, half fille- circles, and T = 189 K, stars) fully merge with measurements. The data are redrawn from Fig. 3b of [13].*

Evidently, the curves calculated under the SCLC assumption (solid triangles: T=295 K, and solid points: T = 189 K), apart for the first and the last data points, strongly deviate at both temperatures from the data of [13] (solid diamonds and solid squares), see Fig. 6. The disagreement indicates the complete absence of the SCLC regime within the ITO/α-NPD/Pd structure; consequently the contact in question is at most quasi-ohmic.

Eq. (2.1) in conjunction with the measured current density, j, [13], is then used to calculate Eint as a function of Ea, The obtained bias dependence of Eint is to a very good approximation described by the temperature-sensitive, 6-th order (inverted) distorted parabola, Table 1, see Fig. 7 (T = 295 K solid dots, and T = 189 K filled diamonds). Then, using the extracted Ea dependent interfacial electric field, Eint, see Fig. 7, together with the appropriate value of the (constant) maximum hole mobility in Eq. (2.1) the recalculated hole current density, j, at each temperature practically coincides with the measured data. This is shown in Fig. 6 exhibited by the thin curve through the calculated points that all coincide with the measurements.
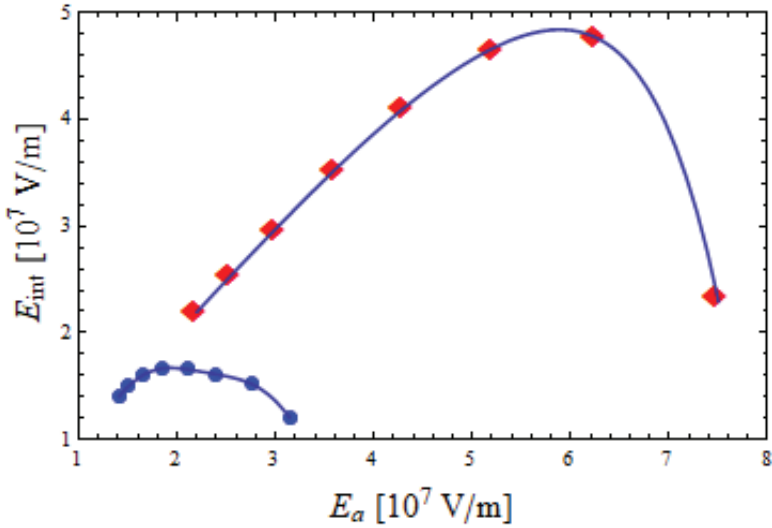
Figure 7: *The calculated electric field at the hole-injecting ITO/α-NPD interface, E_{int}, as a function of the applied electric field, E_a, is exhibited for cases of the ITO/α-NPD(100 nm)/Pd hole j - E_a data of [13]. The approximation functions of the calculated interfacial field at T = 295 K (solid dots) and T = 189 K (diamonds) are given in Table 1, and are represented by thin curves in Fig. 7. No traces of SCLC can be observed.*

The room temperature zero-field mobility at T = 295 K of approximately $\mu0 \sim 1 \times 10\text{-}9$ m2/Vs but for L = 200 nm sample is reported in [13]. The maximum hole mobility for the stated sample analyzed using Eq. (2.2), turns out to be $\mu max = 7.0 \times 10\text{-}10$ m2/Vs (initial Eint = 5.6 MV/m). Consequently, μmax and the zero-field prefactor, $\mu0$, of the conventional exponential mobility remain comparable, [11] even in cases of a minor deviation from the ideal SCLC condition. Consequently, the zero-field prefactor, $\mu0$, and the maximum hole mobility, μmax, appear to be closely related under the SCLC occurrence. Since the latter parameter is strongly temperature-dependent and of the electrode/organic deposition method dependent quantity (as reflected in Eint, see Fig. 7) it is clear that the attempts of fitting various temperature-dependent current-density spectra by the single zero-field prefactor should be unsuccessful, [13].

In Fig. 8, the hole drift mobility for the room temperature structure of [13] is shown (solid dots). In comparison to Fig. 4, its Ea dependence evolves on considerably lower level on account of the smaller value of the maximum hole mobility, μmax, due to the non-ohmic contacts. This occurs despite the fact that the bias-dependent interfacial electric field, Eint, (solid dots, Fig. 7) is about an order of magnitude above the one determined at the room temperature; compare Fig. 2.

For L = 200 nm organic at T = 192 K (the bias independent) maximum hole mobility is found to be $\mu max = 5 \times 10\text{-}11$ m2/Vs at Eamax = 75 MV/m (the postulated SCLC curve is calculated with fixed Eint = 15.1 MV/m). As seen, the maximum hole mobility in α-NPD organic is thickness dependent in agreement with [11], but bias independent.
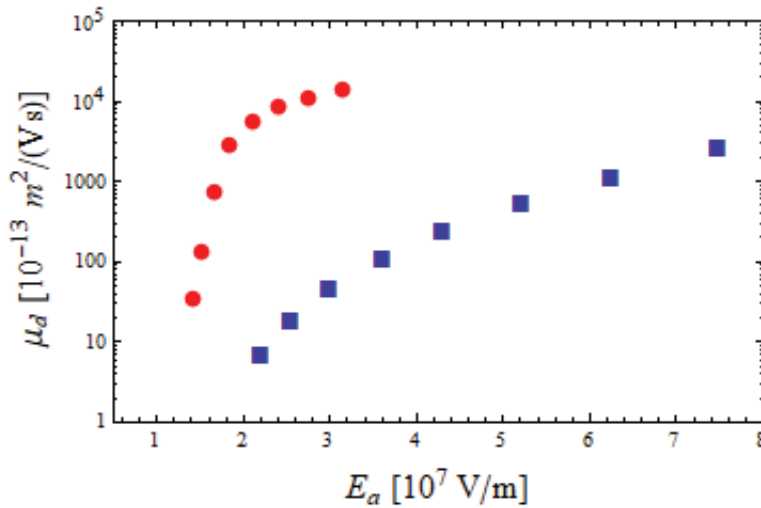
Figure 8: *The E_a dependence of the calculated hole drift mobility, μ_d, Eq. (2.2) at T = 295 K (solid dots), and T = 189 K (solid squares) within the ITO/α-NPD(100 nm)/Pd structure of [13] is shown.*

Based on the analyses above and in conjunction with [11] it is seen that the current density to be characterized as SCLC then the measurements should satisfy Eq. (2.1) where the parameter Eint, the electric field at the hole-injecting electrode/organic interface, ought to remain constant over the wide span of the applied electric field Ea. If a pair of suitably determined bias independent parameters Eint and µmax cause the calculated curve, Eq. (2.1), to intersect just the first and the last data point in the j – Ea diagram this indicates: (a) that the electric field at the hole-injecting interface is bias-dependent, (b) that the operation of a given organic structure is limited to the quasi-ohmic region, and (c) that the maximum hole mobility would necessarily be smaller than the (optimal) one deduced under the SCLC conditions. This is well illustrated in Figs. 4, and 8.

As seen, compare Figs. 4, and 8, the (relatively) highest level of the Ea dependent hole drift mobility, µd, that is then accompanied by the minimal value of the interfacial electric field for a given electrode/organic structure is obtained for SCLC regime at room temperature. The above-presented examples and other similar observations point out the facts that the decrease in temperature is accompanied by the decrease of the hole drift mobility for over one order of magnitude that is simultaneously accompanied by the strong increase in the magnitude of the electric field at the hole-injecting electrode/α-NPD interface. The large electric field at the hole-injecting interface then implies the existence of a considerable hole barrier.

Consequently, on this account, it is claimed that the hole-drift mobility within α-NPD bulk at T = 295 K is µd = 4.4×10-8 m2/(Vs) (at Ea = 25.0 MV/m). It may now be claimed that the value µd = 7.0×10-10 m2/(Vs) (at Ea = 31.4 MV/m) determined from the data of [13] at similar temperature, points to the contact incapability to attain the regions of mobility saturation. Similar observations are valid for measurements obtained at other temperatures.

The excellent agreement between the temperature and bias-dependent measurements of [13] and the predictions of Eq. (2.1), see Fig. 6 (thin curves), is a confirmation that the electric field at the hole-injecting ITO/α-NPD organic interface is at all temperatures strongly Ea dependent. The Ea dependence of electric fields at the stated interfaces, Eint, are all distinct and suitably described in terms of the different (inverted, higher order) parabola-like curves, see Table 1. No real SCLC can be detected in the data of [13] for any thickness and temperature.

At this point it should be emphasized that the data of [12], and [13] are to an excellent approximation described by Eq. (2.1) in terms of two physical clearly defined parameters Eint, and μmax. The stated data are also well- interpreted in terms of the hole transport among the disordered energy states within α-NPD organic medium described in terms of the Gaussian distribution, characterized by its width σ [12, 13]. Consequently, it remains to show that a relationship exists between Eq. (2.1) and the disordered energy states within the organic side of the interface at the hole-injecting electrode/organic junction. This will be accomplished on the basis of a simple model as expressed by Eq. (2.7).

Eq. (2.7) is applied to Eint deduced at T = 189 K, Fig. 6 (the starting value Eint = 23.37 MV/m at maximum Ea = 74.9 MV/m, see Fig. 7 (diamonds), with σ initially set to σ = 0.10 eV. This choice enables the direct comparison with results of [13] to be made. From Eq. (2.7) calculated corresponding energy shift turns out to be φ = 0.719 eV. In the next step the higher value of Eint = 47.64 MV/m evaluated at the lower Ea = 62.5 MV/m, Fig. 7 (diamonds), is balanced by keeping σ unchanged (filled squares) and allowing φ (filled stars) to decrease, see Fig. 9. Then the new value of the (decreased) energy shift φ = 0.697 eV is obtained in the calculation. In subsequent steps this value of the energy shift was kept constant. Namely, it appears unlikely that Gaussian peak could undergo an additional energy shift at still lower values of Ea. Consequently, in the subsequent calculations the parameter φ is kept constant but σ then decreases. The value of Eint = 21.96 MV/m corresponds to the initial Ea = 21.99 MV/m, see Fig. 7 (diamonds) for which σ = 0.0915 eV is found at constant φ = 0.697 eV. The results are presented on Fig. 9.

Starting once again with an arbitrary selected σ = 0.10 eV for Gaussian width, and L* = 5 nm, then similar results are obtained in the analyses of the Eint at T = 295 K, see Fig. 7 (solid dots) that exists at ITO/α-NPD organic structure. The results of the calculations are exhibited in Fig. 9. As seen at σ = 0.10 eV (diamonds) the energy shift φ (triangles) is at T = 295 K equal to φ = 0.763 eV and both parameters are considerably greater than the corresponding values calculated at lowest T. Both parameters are monotonically dependent on the externally applied electric field, Ea, and are single-valued functions of Ea, within the entire experimental region.
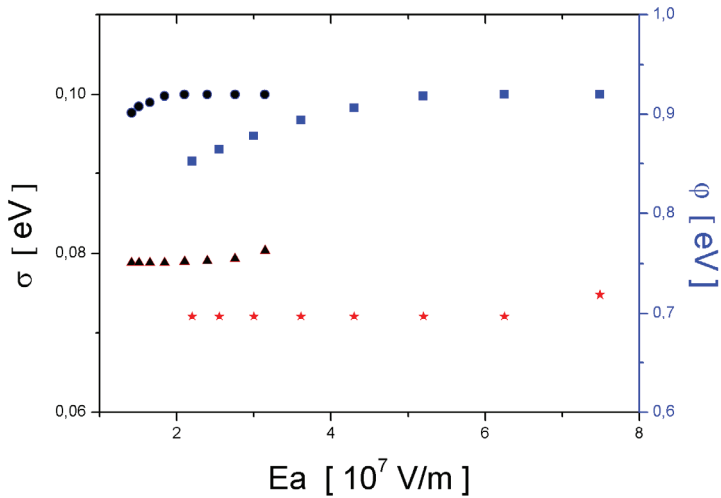
Figure 9: *The E_a dependence of the Gaussian width σ, (left ordinate) calculated from Eq. (2.7) for the values of E_{int} that are shown on Fig. 7: T = 189 K (filled squares), and T = 295 (diamonds) is exhibited. The E_a dependence of the energy shift φ (right scale) of Gaussian peak is presented for T = 189 K (filled stars) and T = 295 K (triangles).*

It is seen that the parameter σ = 0.10 eV for Gaussian width that has been determined by CDM results in [13] provides through Eq. (2.7) a self-consistent description of the double-valued Eint as a function of Ea under the condition that the Gaussian width, σ, and the energy shift of its peak, φ, are bias-dependent. Consequently, under the stated constraint the compatibility of Gaussian model derived parameter of [13] to the predictions of Eq. (2.7) has been demonstrated.

Their analyses have shown that the data cannot be consistently interpreted in terms of the drift-diffusion model incorporating the conventional exponential bias-dependent hole mobility. This inability was attributed to the fact that the dependence of the hole mobility on charge density is neglected in the stated model.

In this section, the hole drift transport within the disordered organic states has also been indirectly verified. It was shown that the experimentally determined interfacial electric field at the hole-injecting interface, Eint, is on the basis of a simplified model, well interpreted by the (Ea dependent) parameters of [22] that characterize Gaussian distribution of the disordered energy states within the α-NPD organic as reported [12, 13]. It was shown that such relationship exists irrespective of the current density being of SCLC type or not. Since by Eq. (2.2) the interfacial field, Eint, critically affects the hole drift mobility, μ_a, compare Figs. 4 and 8, the relationship between the hole drift mobility, μ_d, and Gaussian disordered states is revealed.

Returning to Figs. 4, and 8 the minimum value of the evaluated room temperature hole drift mobility for TCTA/α-NPD interface of [12] turns out to be μ_{dmin} = 3.8×10-8 m2/(Vs) at Eamin = 1.94 MV/m. The corresponding (minimum) value of μ_d determined for ITO/α-NPD interface of [13] is found to be μ_{dmin} = 1.7×10-12m2/(Vs) at Eamin = 14.12 MV/m. Evidently, the effect of the electrode/α-NPD electrical contact on the hole drift mobility is most instructive. The reason

for almost four orders of magnitude between the two is traced to the existence of considerably different electric fields at the stated contacts as exhibited in Fig. 2, and Fig. 7.

As seen, Eq. (2.1) enables that the interfacial electric field, Eint, be determined directly from the measured current-voltage data. This implies that the hole current density, j, as a function of Ea implicitly incorporates the hole density Ea dependence and, for this reason, the stated effect on the deduced hole drift mobility is redundant. Likewise, the effect of the built-in voltage is at all times expected to be compensated by the corresponding part of the charge density induced at the interface and, consequently, it is expected not to have any specific role in the steady-state current-voltage determination of Eint as a function of bias, Ea.

4   CONCLUSIONS

In the present work, based upon the published current-voltage data, the influence of the electric field at the hole-injecting electrode/α-NPD organic structure on the hole transport has been investigated. It is shown that the (steady-state) hole drift current density within the organic structure crucially depends on two experimentally deduced parameters: the electric field at the hole-injecting electrode/organic interface, Eint, and the so-called maximum drift mobility, μmax. It is empirically verified that, in a given experiment, μmax, is a fixed constant, but the interfacial electric field, Eint, could be a function of the externally applied electric field, Ea. It is argued that hole drift SCLC occurs whenever the stated electric field, Eint, is over a given interval of the externally applied electric field, Ea a fixed small constant (with respect to Ea). Then, the hole drift mobility is prone to attain (weakly) bias-dependent saturation that represents an optimum for the organic structure under the investigation. If the data cannot be described by the constant Eint then its bias dependence may be calculated, and its detrimental effect on the hole drift mobility is clearly exhibited. It is revealed that merely by increasing externally applied electric field, the non-SCLC occurring due to the quasi-ohmic contact of the electrode/α-NPD interface may transcend into the ohmic one. It is shown that the different electric fields that originate at the hole-injecting electrode/α-NPD interfaces are closely related to vastly different values of the hole drift mobility within the chemically identical α-NPD organic.

On the assumption that the interface may be described in terms of an infinite thin uniformly charged sheet, then the relationship between Eint and the Gaussian distribution of the disordered energy states within the α-NPD organic interface is established. It is shown that the Gaussian width and the energy shift of its central position along the negative binding energy are Ea dependent.

Based on the described findings, it appears that the current-voltage method might serve as a useful tool for probing the electric fields at charge injecting/organic interfaces.

References

[1] **K. H., S. Y. Yang, C. Yang, S. H. Kim, D. Choi, C. E. Park:** *Reducing the contact resistance in organic thin-film transistors by introducing a PEDOT:PSS hole-injection layer,* Org. Electron. **9,** 864, 2008

[2] **Z. Liu, M. Kobayashi, B. C. Paul, Z. Bao, Y. Nishi**: *Contact engineering for organic semiconductor devices via Fermi level depinning at the metal-organic interface,* Phys. Rev. B, **82**, 035311, 2010

[3] **N. B. Kotadiya, H. Lu, A. Mondal, Y. Ie, D. Andrienko, P. W. M. Blom, G.-J. A. H. Wetzelaer**: *Universal strategy for Ohmic hole injection into organic semiconductors with high ionization energies,* Nature Materials, **17,** 329, 2018

[4] **A. A. Günther, M. Sawatzki, P. Formánek, D. Kasemann, K. Leo**: *Contact Doping for Vertical Organic Field-Effect Transistors,* Adv. Funct. Mater. **26,** 768, 2016, DOI: 10-1002/adfm.201504377

[5] **W.-L. Seah, C. G. Tang, R.-Q. Png, V. Keerthi, C. Zhao, H. Guo, J.-G. Yang, M. Zhou, P. K. H. Ho, L.-L. Chua**: *Interface Doping for Ohmic Organic Semiconductor Contacts Using Self-Aligned Polyelectrolyte Counterion Monolayer,* Adv. Funct. Mat. **27,** 1606291, 2017

[6] **C. Liu, Y. Xu, Y.-Y. Noh**: *Contact engineering in organic field-effect transistors,* Materials Today **18,** 79, 2015

[7] **S. Liu, P. Billig, A. Al-Shadeedi, V. Kaphle, B. Lüssem**: *Doped bottom-contact organic field effect transistors,* Nanotechnology **29,** 284001, 2018

[8] **Z. B. Wang, M. G. Helander, M. Greiner, J. Qui, Z. H. Lu**: *Analysis of charge-injection characteristics at electrode-organic interfaces: Case study of the transition-metal oxides,* Phys. Rev. B **80,** 235325, 2009

[9] **Z. B. Wang, M. G. Helander, M. T. Greiner, J. Qui, Z. H. Lu**: *Carrier mobility of organic semiconductors based on current-voltage characteristics,* J. Appl. Phys. **107,** 034506, 2010

[10] **J. C. Blakesley, F. A. Castro, W. Kylberg, G. F. A. Dibb, C. Arantes, R. Valaski, M. Cremona, J. S. Kim, J.-S. Kim:** *Towards reliable charge-mobility benchmark measurements for organic semiconductors,* Org. Electron.*,* **15,** 1263, 2014

[11] **B. Cvikl:** *The electric field at hole injecting metal/organic interface as a cause for manifestation of exponential bias-dependent mobility,* Thin Solid Films **573,** 56, 2014

[12] **R. Rohloff, N. B. Kotadiya, N. I. Craciun, P. W. M. Blom, G. A. H. Wetzelaer:** *Electron and hole transport in the organic small molecule α-NPD,* Appl. Phys. Lett. **110,** 073301, 2017

[13] **S. L. M. van Mensfoort, V. Shabro, R. J. de Vries, R. A. Janssen, R. Coehoom**: *Hole transport in the organic small molecular material α-NPD; evidence for the presence of correlated disorder,* J. Appl. Phys. **107,** 113710 2010

[14] **M. A. Lampert**: *Simplified Theory of Space-Charge-Limited-Currents in an Insulator with Traps,* Phys. Rev. **103,** 1648, 1956

[15] **P. Mark, W. Helfrich**: *Space-Charge-Limited Currents in Organic Crystals,* J. Appl. Phys. **33,** 205, 1962

[16]   **S. Nishi, D. Taguchi, T. Manaka, M. Iwamoto**: *Analysis of current-voltage characteristics of Au/pentacene/fluorine polymer/indium zinc oxide diodes by electric-field-induced-optical second-harmonic generation,* J. Appl. Phys. **117,** 245502, 2015

[17]   **D. Taguchi, L. Zhang, J. Li, M. Weis, T. Manaka, M.. Iwamoto**:, *Analysis of Carrier Transients in Double-Layer Organic Light Emitting Diodes by Electric-Field-Induced Second-Harmonic Generation Measurement,* J. Phys. Chem. C, **114,** 15136, 2010

[18]   **W. F. Pasveer, J. Cottaar, C. Tanase, R. Coehoorn, P. A. Bobbert, P. W. M. Blom, D. M. de Leeuw, M. A. J. Michels**: *Unified Description of Charge-Carrier Mobilities in Disordered Semiconducting Polymers,* Phys. Rev. Lett. **94,** 206601, 2005

[19]   **M. M. Mandoc, B. de Boer, G. Paasch, P. W. M. Blom:** *Trap-limited electron transport in disordered semiconducting polymers,* Phys. Rev. B **75,** 193202, 2007

[20]   **M. Bouhassoune, S.L.M. van Mensfoort, P.A. Bobbert, R. Coehoorn**: *Carrier-density and field-dependent charge-carrier mobility in organic semiconductors with correlated Gaussian disorder,* Org. Electron. **10,** 437, 2009

[21]   **I. Lange, J. C. Blakesley, J. Frisch, A. Vollmer, N. Koch, D. Neher**: *Band Bending in Conjugated Polymer Layers,* Phys. Rev. Lett. **106,** 216402, 2011

[22]   **M. Oehzelt, N. Koch, G. Heimel**: *Organic semiconductor density of states controls the energy level alignment at electrode interfaces,* Nat. Commun. **5** 4174, 2014

[23]   **Y. Shen, M. W. Klein, D. B. Jacobs, J. C. Scott, G. G. Malliaras**: *Mobility-Dependent Charge Injection into an Organic Semiconductor*, Phys. Rev. Lett. **86,** 3867, 2001

[24]   **T. J. Whitcher, W. S. Wong, A. N. Talik, K. L. Woon, N. Chaniek, H. Nakajima, T. Saisopa, P. Songsiriritthigul**: *Electrostatic model of energy-bending within organic semiconductors: experiment and simulation*, J. Phys.: Condens. Matter **28,** 365002, 2016

[25]   **T. J. Whitcher, W. S. Wong, A. N. Talik, K. L. Woon, N. Chaniek, H. Nakajima, T. Saisopa, P. Songsiriritthigul**: *Investigation into the Gaussian density of states widths of organic semiconductors,* J. Phys. D: Appl. Phys. **49,** 325106, 2016.

[26]   **M. S. Khoshkhoo, H. Peisert, T. Chassé, M. Scheele**: T*he role of the density of interface states in interfacial energy level alignment of PTCDA*, Org. Electron. **49,** 249, 2017

[27]   **S. Beck, D. Gerbert, T. Glaser, A. Pucci**: C*harge Transfer at Organic/inorganic Interfaces and the Formation of Space Charge Regions Studied with Infrared Light*, J. Phys. Chem. *C* **119,** 12545, 2015

[28]   **G. Jecl, B. Cvikl**: *The density-of-states contributions to the negative field charge drift mobility effect in poly(3-hexylthiopene) organic semiconductor,* Thin Solid Films*,* **646,** 190, 2018

[29]   **T. Matsushima, Y. Kinoshita, H. Murata**:, *Formation of Ohmic hole injection by inserting an ultrathin layer of molybdenum trioxide between indium tin oxide and organic hole-transport layer,* Appl. Phys. Lett. **91,** 253504, 2007

Journal of
Energy
Technology

A REVIEW OF HYBRID PHOTOVOLTAIC/ THERMAL SYSTEMS

PREGLED HIBRIDNIH TERMOELEKTRIČNIH SISTEMOV

Klemen Sredenšek [1ℜ], Sebastijan Seme [1,2]

Keywords: photovoltaic/thermal systems, collector type, coolant type, electrical/thermal efficiency

Abstract

The primary objective of this paper is to review state-of-the-art hybrid photovoltaic/thermal systems and their performance analysis. The paper is designed to facilitate the comparison and evaluation of results obtained by other authors. The review was carried out for different types and designs of photovoltaic/thermal modules in indoor and outdoor conditions, as well as for different cooling types and materials.

Povzetek

Cilj prispevka je pregled stanja hibridnih termoelektričnih sistemov in njihove učinkovitosti delovanja. Struktura prispevka je tematsko zasnovana tako, da olajša primerjavo in ovrednotenje rezultatov med drugimi študijami. Pregled je izveden za različne tipe in oblike termoelektričnih modulov, ter za različne vrste hlajenja in uporabljenih materialov.

ℜ Corresponding author: Klemen Sredenšek, M.Sc., E-mail address: klemen.sredensek@um.si

[1] University of Maribor, Faculty of Energy Technology, Hočevarjev trg 1, 8270 Krško, Slovenia

[2] University of Maribor, Faculty of Electrical Engineering and Computer Science, Koroška cesta 46, 2000 Maribor, Slovenia, e-mail: sebastijan.seme@um.si

1   INTRODUCTION

Life depends primarily on energy and its consumption. Due to population growth, the electrification of transport and many other aspects, the development of new technologies for extracting energy from renewable sources is of utmost importance. The share of renewables in total final energy consumption (TFEC) grew by an estimated 0.25%, to around 19% of TFEC by 2017. The world needs to increase the share of renewable energy in TFEC from 19% to 65% by 2050, *[1]*. The share of photovoltaic systems (PV) increased dramatically over the previous decade, and their total installed capacity exceeded the sum of all other renewables. The efficiency of PV modules depends mainly on the density of solar radiation, *G*, and the temperature of PV module *T*. Hybrid photovoltaic/thermal systems have been developed that simultaneously increase the efficiency of the PV module and use excess heat in heating applications.

Given that PV/T modules produce more energy per unit area than PV and thermal modules separately, these systems are particularly suitable for applications where the available surface area is limited *[2]* and will play an essential role in the near future. Over the past thirty years, a great deal of research has been carried out by researchers on the concept of module type, coolant type and materials suitable for PV/T systems. Therefore, the next three chapters will briefly outline the findings and current use of PV/T systems, which has been already done by other authors of PV/T review papers. Figure 1 shows a simplified schematic of the PV/T module connected to a water storage tank.
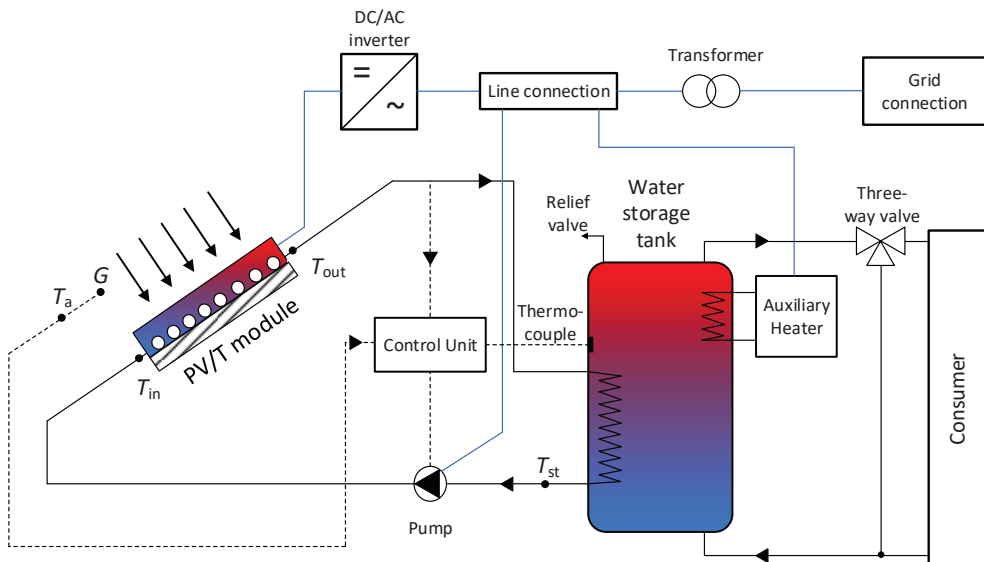

***Figure 1:** A simplified scheme of PV/T system.*

2   HYBRID PHOTOVOLTAIC/THERMAL SYSTEM

Hybrid PV/T systems simultaneously convert solar energy into electrical and thermal energy. Excess heat that reduces the electrical efficiency of the PV module is discharged via the coolant to the heat storage tank. The PV/T system is divided into module type, coolant type, and PV material type, presented in Figure 2. The PV/T system can be optimized by setting the operating point at which the module will simultaneously produce more electrical energy and enough thermal energy. The operation is monitored by a unit that controls the mass flow rate of the coolant, via the inlet and outlet temperatures of the PV/T module.
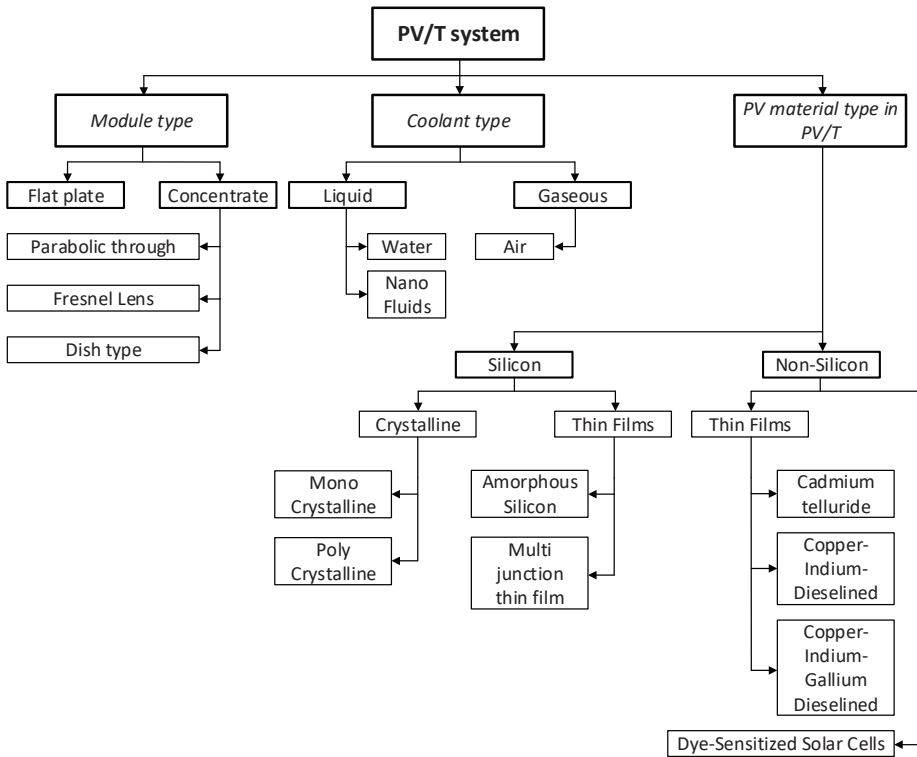
Figure 2: *Schematic division of PV/T modules (redrawn from [3]).*

3   MODULE TYPE

3.1   Concentrating PV/T modules

According to the concentration ratio (CR), the concentrating PV or PV/T systems can be divided into low-concentrating systems and high-concentrating systems with an additional tracking system. Under high concentration ratios, for instance, a multidisc concentrator with 150

concentration ratios, the PV system has a severe cooling problem, *[4]*. Jaaz et al., *[5]*, presents a performance analysis of a PV/T module using water jet impingement and compound parabolic concentrator (CPC). Since the electrical efficiency and output power are directly correlated with the mass flow rate, the system can be improved by using jet impingement of water to decrease the temperature of the PV module. The results show that electrical efficiency was improved by 7% when using CPC and jet impingement cooling, while the output power was improved by 36% when using jet impingement cooling with CPC, and 20% without CPC. In his second study, *[6]*, the results of power output and electrical efficiency were very similar, while thermal efficiency improved to 81%. Singh et al., *[7]*, performed an enhanced experimental study on concentrating PV/T air collector with fresnel lenses and CPC, based on previously applied studies and methodologies. The results showed that the highest electrical and thermal efficiencies of the concentrating PV/T collector were found to be 12.9% and 50%, while a total combined efficiency was 80%. The average solar radiation, mass flow rate, and geometric concentration ratio were 750 W/m^2, 0.03 kg/s, and 1.78, respectively.

3.2   Flat-plate PV/T modules

Flat-plate PV/T modules first appeared in 1978, *[8]*, and represent the most commercially successful type of PV/T modules. Flat-plate PV/T collectors can be divided according to the type of the used working fluid: water type, *[9-17]*, air type, *[18-20]*, and water/air type, *[21]*. Das et al., *[22]*, presents a review on the design and development of flat plate hybrid PV/T systems. According to the full review of the literature, the authors found that the sheet-and-tube is the most dominant thermal absorber fabrication technique when heat transfer fluid is a liquid, that the phase change material (PCM) based PV/T modules has immense potential to be integrated into building facades, and that the graphite infused PCM significantly enhances the electrical efficiency of PV module.

4   COOLANT TYPE

4.1   Water PV/T modules

The most useful working fluid in PV/T systems is undoubtedly water, as it has a higher thermal conductivity, heat-carrying capacity, and heat transfer rate than air, and thus provides more uniform cooling of the PV module. In addition to the working fluid, the design of the sheet-and-tube, which is usually installed on the back of the PV/T module, is also extremely important. Abdulameer et al., *[9]*, investigated the performance of two different types of sheet-and-tube PV/T module (serpin-direct and serpentine sheet-and-tube design), changing the mass flow rate. The results showed that the serpin-direct sheet-and-tube design achieved better electrical efficiency (by 0.4%), with a mass flow of 0.1 kg/s and solar radiation of 900 W/m^2. In summary, the mass flow rate plays an essential role in the design of PV/T modules. Nowzari, *[11]*, numerically investigated the performance of six different configurations of sheet-and-tube design on the PV module, with heat flux and output temperature representing the output parameters. The first four models represent a channel of different thicknesses mounted on the front or back of the PV module, while the last two models represent a channel with fins of different thicknesses mounted on the back of the PV module. The results showed that the first model with a front-mounted water channel had the highest amount of heat flux and, therefore,

backside of a monocrystalline silicon PV module. As previous studies have shown, mass flow is critical as it changes the outlet temperature of the water from the sheet-and-tube collector and, consequently, the thermal efficiency of the PV/T module. However, since mass flow is also related to electrical efficiency (faster cooling), it is necessary to determine the optimal mass flow rate of the system to achieve relatively high thermal and electrical efficiency at the same time. Therefore, the study, *[12]*, investigates the optimum mass flow rate of a PV/T system, while also taking into account the most optimal slope and volume of water in the system. In addition, the results of the experiment showed that the PV/T module produces an excellent performance at a range of 0.10–0.15 kg/s mass flow rate, as well as, 100 l water volume and 25° inclination angle. Figure 3 presents the schematics of the various PV/T water/air modules; a) air-flow before PV module and water flow in the tube (commercial type of water cooling), b) air/water flow (separated) before PV module, c) air/water flow (combined) before PV module and d) air/water flow (separated) before PV module and air/water flow (combined) behind PV module.
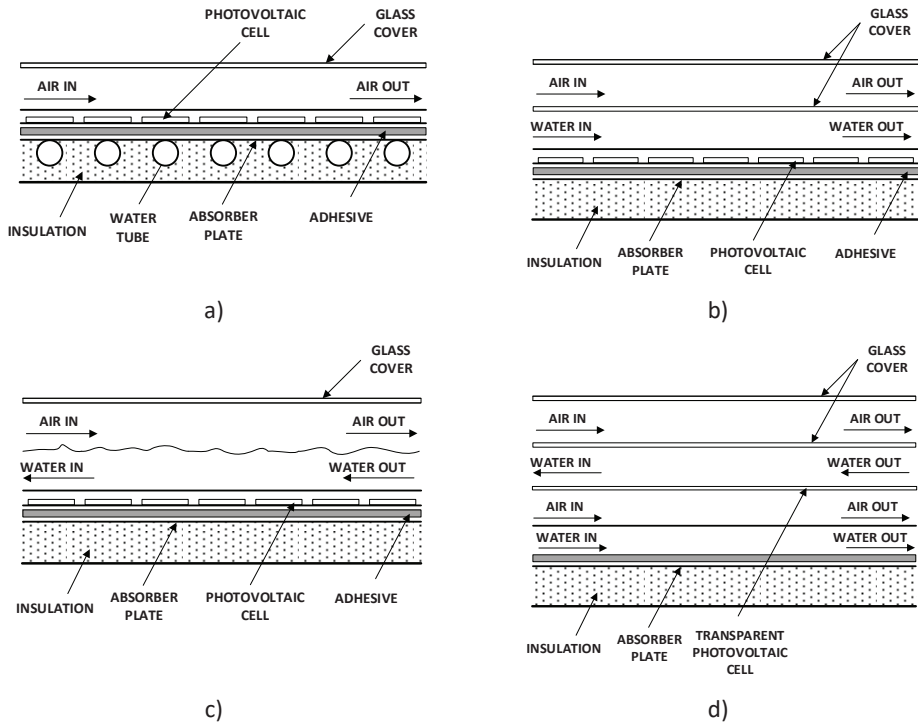

Figure 3: *Schematics of the various PV-T air/water modules (redrawn from [1]): a) airflow before PV module and water flow in the tube (commercial type of water cooling), b) air/water flow (separated) before PV module, c) air/water flow (combined) before PV module and d) air/water flow (separated) before PV module and air/water flow (combined) behind PV module.*

In addition to the described systems, there are also interesting features, such as adding iron filings between sheet-and-tube water module and absorbing plate to increase the heat transfer between the working fluid and PV module, *[13]*. An experimental study presented by Huo, *[13]*, shows that the temperature of the PV module is effectively reduced by filling iron chip (from 3.5 to 6.5 ° C), thus increasing the electrical efficiency to 19.8%. Cen et al., *[14]*, presents an experimental study on a direct water heating PV/T technology as a self-powered, off-grid, solar system. The PV/T system demonstrated the ability to provide hot water (approx. 80 °C) for a family of four, as well as providing excess electricity for household applications (average solar radiation of 4.5 kWh/m^2), with electrical and thermal efficiency of 13.4 and 53.4 %, respectively. Seme et al., *[23]*, present a research study of various designs of sheet-and-tube PV/T water modules and measurements of the flat-plate PV/T water module of the German manufacturer WIOSUN. The PV/T system is presented in Figure 4 and consists of a flat-plate PV/T water module, heat pump (evaporator/compressor/condenser) and convector. On its primary side, a flat-plate PV/T module uses solar glycol as a working fluid, while the secondary side uses water. Figures 5 and 6 present the output power and efficiency of the PV module as a function of the temperature of the PV module *T* and solar radiation *G*. The results show that cooling the PV/T module to 10 °C improves the output power and efficiency by approximately 10% and 2%, respectively.

Figure 4: *PV/T system of a German manufacturer WIOSUN: 1. Silicon poly-crystalline PV/T water module, 2. heat pump (evaporator/compressor/condenser), 3. Convector, [23].*
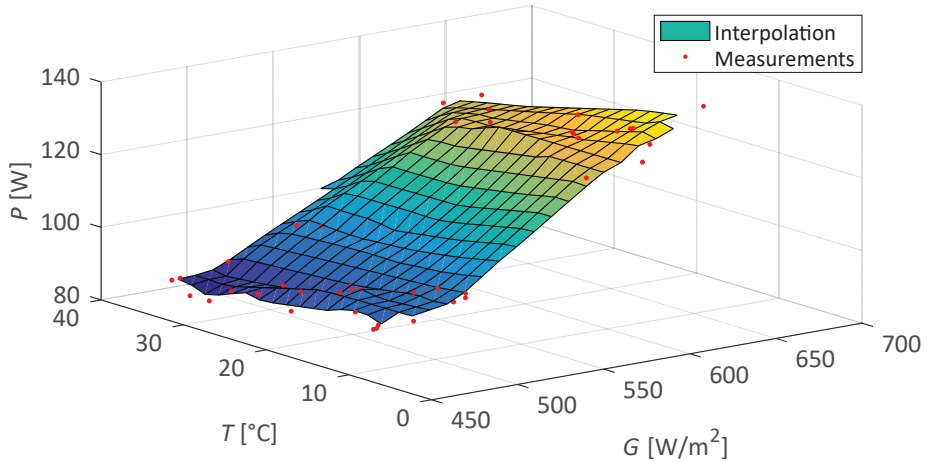
Figure 5: *The output power P, as a function of the temperature of the PV module T and solar radiation G (results used from [23]).*
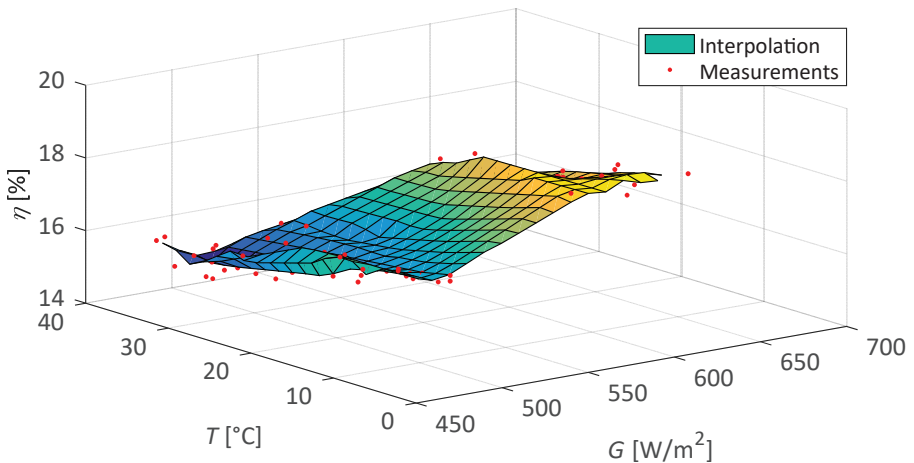

Figure 6: *The efficiency of the PV module, as a function of the temperature of the PV module T and solar radiation G (results used from [23]).*

4.2   Air PV/T modules

In addition to the disadvantages, the air PV/T module also has enormous advantages over the water PV/T module: simplicity in construction, low operational cost and suitability for integration into buildings, *[24]*. Furthermore, it is suitable for implementation in areas with lower temperatures. Saygin et al., *[19]*, present an experimental study of a modified PV/T air module, with air entering the module through a gap in the middle of the glass cover.

Measurements were taken for 3 different distances (3, 5 and 7 cm) of the glass cover from the PV module, at different tilt angles and mass flow rates. The highest thermal efficiency was obtained at a distance of 3 cm between the glass cover and the PV module, while the electrical efficiency was obtained at a distance of 5 cm. Hussain et al., *[20]*, present a review paper of design development and performance evaluation of PV/T air modules, highlighting recent developments of PV/T modules and studies that present the integration of photovoltaic/thermal air (BIPV/T) systems into buildings. Figure 7 presents the schematics of the various PV/T air modules; a) airflow before PV module, b) airflow behind PV module, c) and d) before and behind PV module.
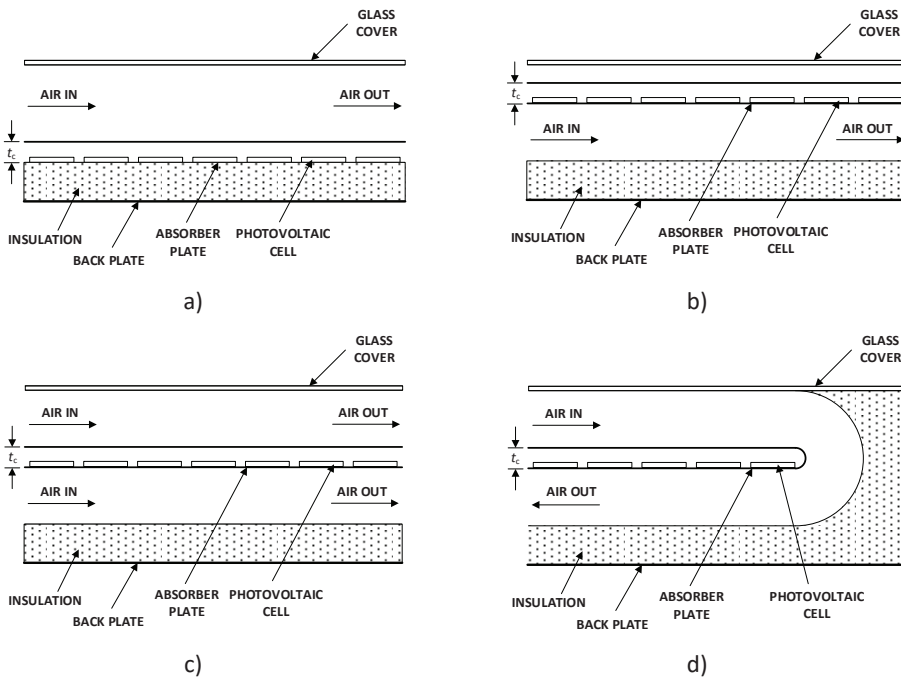

Figure 7: Schematics of the various PV/T air modules (redrawn from [25]): a) airflow before PV module, b) airflow behind PV module, c) and d) before and behind PV module.

5   CONCLUSION

This paper aims to present state-of-the-art hybrid PV/T systems; it describes the basic methodology, advantages and disadvantages of individual technologies and coolants. The results of studies presented by other authors have shown that the commercialization of PV/T systems is not growing as fast as individual photovoltaic or thermal systems. Given that PV/T modules represent greater potential due to high efficiency per unit area, it can be expected that the development will increase and thus reduce the production and installation costs in the near future. In further development, nanoparticles will play an important role as they have even

problem of the sedimentation of nanoparticles in case of PV/T system failure (consequence: reduction of thermal conductivity).

References

[1]   **IRENA - International Renewable Energy Agency**: *Global Energy Transformation: A roadmap to 2050*, Abu Dhabi, 2018

[2]   **F. Calise, R. D. Figaj, L. Vanoli**: *Experimental and Numerical Analyses of a Flat Plate Photovoltaic/Thermal Solar Collector*, Energies, Vol. 10, Iss. 491, p.p. 1 – 21, 2017

[3]   **C. Babu, P. Ponnambalam:** *The role of thermoelectric generators in the hybrid PV/T systems: A review,* Energy Conversion and Management, Vol. 151, p.p. 368 – 385, 2017

[4]   **S. M. Sultan, M. N. E. Efzan:** *Review on recent Photovoltaic/Thermal (PV/T) technology advances and applications*, Solar Energy, Vol. 173, p.p. 939 – 954, 2018

[5]   **A. H. Jaaz, H. A. Hasan, K. Sopian, A. A. H. Kadhum, T. S. Gaaz, A. A. Al-Amiery:** *Outdoor Performance Analysis of a Photovoltaic Thermal (PVT) Collector with Jet Impingement and Compound Parabolic Concentrator (CPC)*, Materials, Vol. 10, Iss. 888, p.p. 1 – 16, 2017

[6]   **A. H. Jaaz, K. Sopian, T. S. Gaaz:** *Study of the electrical and thermal performances of photovoltaic thermal collector-compound parabolic concentrated*, Results in Physics, Vol. 9, p.p. 500 – 510, 2018

[7]   **B. S. S. Singh, C. H. Yen, S. H. Zaidi, K. Sopian:** *Part II: Enhanced Performance of Concentrating Photovoltaic-Thermal Air Collector with Fresnel Lens and Compound Parabolic Concentrator (CPC)*, Journal of Advanced Research in Fluid Mechanics and Thermal Sciences, Vol. 47, Iss. 1, p.p. 16 – 24, 2018

[8]   **E. C. Kern, M. C. Russell:** *Combined photovoltaic and thermal hybrid collector systems*, 13th IEEE Photovoltaic Specialists Conference, Washington DC, USA, 5 – 8 June 1978

[9]   **F. Abdulameer, M. A. M. Rosli, N. Tamaldin, S. Misha, A. L. Abdullah:** *Modelling, Validation and Analyzing Performance of Serpentine-Direct PV/T Solar Collector Design*, CFD Letters, Vol. 11, Iss. 2, p.p. 50 – 65, 2019

[10]   **G. Evola, L. Marletta:** *Exergy and thermoeconomic optimization of a water-cooled glazed hybrid photovoltaic/thermal (PVT) collector*, Solar Energy, Vol. 107, p.p. 12 – 25, 2014

[11]   **R. Nowzari:** *Numerical Analysis of a Photovoltaic Module Integrated with Various Water Cooling Systems*, Transactions of FAMENA, Vol. 43, p.p. 19 – 30, 2019

[12]   **W. Panga, Y. Cuib, Q. Zhanga, H. Yua, L. Zhanga, H. Yana**: *Experimental effect of high mass flow rate and volume cooling on performance of a water-type PV/T collector*, Solar Energy, Vol. 188, p.p. 1360 – 1368, 2019

[13]   **Y. Huo, J. Lv, X. Li, L. Fang, X. Ma, Q. Shi:** *Experimental study on the tube plate PV/T system with iron filings filled*, Solar Energy, Vol. 185, p.p. 189 – 198, 2019

[14] **J. Cen, R. Feu, M. E. Diveky, C. McGill, O. Andraos, W. Janssen:** *Experimental study on a direct water heating PV-T technology*, Solar Energy, Vol. 176, p.p. 604 – 614, 2018

[15] **M. Moradgholi, S. M. Nowee, I. Abrishamchi**: *Application of heat pipe in an experimental investigation on a novel photovoltaic/thermal (PV/T) system*, Solar Energy, Vol. 107, p.p. 82 – 88, 2014

[16] **H. Chen, S. B. Riffat, Y. Fu:** *Experimental study on a hybrid photovoltaic/heat pump system*, Applied Thermal Engineering, Vol. 31, p.p. 4132 – 4138, 2011

[17] **G. L. Jin, M. Y. H. Othman, H. Ruslan, K. Sopian**: *Photovoltaic Thermal (PV/T) Water Collector Experiment Study*, Latest Trends in Renewable Energy and Environmental Informatics, p.p. 117 – 124, ISBN: 978-1-61804-175-3 124

[18] **P. Zhang, X. Rong, X. Yang, D. Zhang**: *Design and performance simulation of a novel hybrid PV/T-air dual source heat pump system based on a three-fluid heat exchanger*, Solar Energy, Vol. 191, p.p. 505 – 517, 2019

[19] **H. Saygin, R. Nowzari, N. Mirzaei, L. B. Y. Aldabbagh**: *Performance evaluation of a modified PV/T solar collector: A case study in design and analysis of experiment*, Solar Energy, Vol. 141, p.p. 210 – 221, 2017

[20] **F. Hussain, M. Y. Hothman, K. Sopian, B. Yatim, H. Ruslan, H. Othman**: *Design development and performance evaluation of photovoltaic/thermal (PV/T) air base solar collector*, Renewable and Sustainable Energy Reviews, Vol. 25, p.p. 431 – 441, 2013

[21] **M. Y. Othman, F. Hussain, K. Sopian, B. Yatim, H. Ruslan**: *Performance Study of Air-based Photovoltaic-thermal (PV/T) Collector with Different Designs of Heat Exchanger*, Sains Malaysiana, Vol. 42, Iss. 9, p.p. 1319 – 1325, 2013

[22] **D. Das, P. Kalita, O. Royb:** *Flat plate hybrid photovoltaic- thermal (PV/T) system: A review on design and development*, Renewable and Sustainable Energy Reviews, Vol. 84, p.p. 111 – 130, 2018

[23] **S. Seme, M. Jamnik, M. Garmut, K. Sredenšek, D. Tasić, M. Slatinek, A. Krajnc, J. Jovan, K. Pertinač, N. Pavlič:** *Termoelektrični sončni modul za soproizvodnjo električne in toplotne energije*, Final project report, 2016

[24] **F. Yazdanifard, M. Ameri**: *Exergetic advancement of photovoltaic/thermal systems (PV/T): A review*, Renewable and Sustainable Energy Reviews, Vol. 97, p.p. 529 – 553, 2018

[25] **R. R. Avezov, J. S. Akhatov, N. R. Avezova**: *A Review on Photovoltaic/Thermal (PV–T) Air and Water Collectors*, Applied Solar Energy, Vol. 47, Iss. 3, p.p. 169 – 183, 2011

Nomenclature

(Symbols)	(Symbol meaning)
BIPV/T	building integrated photovoltaic/thermal
CPC	compound parabolic concentrator
CR	concentration ratio
G	solar radiation
PCM	phase change material
PV	photovoltaic
PV/T	photovoltaic/thermal
T	temperature
T_a	ambient temperature
TFEC	total final energy consumption
T_{in}	inlet temperature
T_{out}	outlet temperature
T_{st}	temperature from energy storage tank

Journal of
Energy
Technology

FRACTURE TOUGHNESS OF HSLA WELDS MADE ON PENSTOCK MATERIAL

LOMNA ŽILAVOST HSLA ZVAROV ZGRAJENIH NA JEKLIH ZA VODNE ZAPORNICE

Zdravko Praunseis[R]

Abstract

The presence of different microstructures along the pre-crack fatigue front has a significant effect on the critical crack tip opening displacement (CTOD). This value is the relevant parameter for the safe servicing of welded structures (penstocks). In the case of specimens with the through-thickness notch partly in the weld metal, partly in the heat-affected zone, and partly in the base material, i.e., using the composite notched specimen, the fracture behaviour significantly depends on the portion of the ductile base material, the size, and the distribution of mismatching factor along the vicinity of the crack front.

Povzetek

Prisotnost različnih mikrostruktur na fronti konice utrujenostne razpoke ima pomemben vpliv na odpiranje konice razpoke (CTOD). Ta vrednost je relevantni parameter za varno obratovanje varjenih konstrukcij (vodne zapornice). V primeru preizkušancev z globoko razpoko, kjer fronta konice razpoke zajema del zvara, toplotno vplivanega področja in osnovnega materiala, t.i. kompozitno razpoko v preizkušancih, je lomno obnašanje odvisno od deleža žilavega osnovnega materiala, ter velikosti in porazdelitve faktorja trdnostne neenakosti vzdolž fronte razpoke.

[R] Corresponding author: Associate Professor, Zdravko Praunseis, PhD, Faculty of Energy Technology, University of Maribor, Tel.: +386 31 743 753, Hočevarjev trg 1, Krško, Slovenia, E-mail address: zdravko.praunseis@um.si

1   INTRODUCTION

High strength low-alloyed (HSLA) steels are often used as materials of penstocks at hydroelectric power stations for the build-up of multipass welded joints. The welding of HSLA steels to produce under-matched weld joints is a technological challenge for the production of welded structures.

Under-matched welded joints are used for repairing the welding of joint damage during difficult operation conditions or by short-period overloading, *[1]*. They are recommended for preventing hydrogen cracking with preheating, especially for welded joints made of HSLA steels with yield strengths above 700MPa.

Crack tip opening displacement (CTOD) as a fracture toughness parameter is determined as the lowest toughness of different microstructures along the crack front, according to the weakest link model, *[2-5]*. The development of the microstructure in the weld metal and especially in heat-affected zones (HAZ) of multi-pass joints is strongly influenced by welding thermal cycle and base material properties. Metallographically examined microstructures in undermatched joints with homogeneous and heterogeneous welds are primarily those with expected extremely low fracture toughness.

Therefore, the aim of this paper is to analyse the fracture behaviour of HSLA under-matched welded joints made on penstock material, and also to determine the relevant parameters that contribute to higher critical values of fracture toughness, *[6-8]*.

2   EXPERIMENTAL PROCEDURE

High strength low alloyed (HSLA) steel in a quenched and tempered condition, corresponding to the grade HT 80, was used. The Fluxo Cored Arc welding process (FCAW) was used, and two different tubular wires were selected. Three different types of global undermatched welded joints were produced: one homogeneous and two heterogeneous. Homogeneous welded joints were made with pre-heating and post-heating of the base material, entirely with the same consumable. Two different types of heterogeneous welded joints were made using a softer consumable for the soft root layer, one with two and the other with four passes, in order to avoid preheating of the base material and to prevent cold cracking. Defects in the welded joints were detected using the Non-Destructive Method (NDM), *[1]*. Radiography was used, and defects were classified according to the International Standard IIW, *[4]*.

The basic mechanical properties of multi-pass undermatched joints with homogeneous and heterogeneous welds are obtained using round tensile specimens, extracted from the weld metal in the welding direction, from filler passes and the root weld metal region, *[8]*.

In addition to the global strength mismatch between weld metal and base material In the undermatched joint with the homogeneous and heterogeneous welds, a local strength mismatch between the weld metal and HAZ and root weld metal and weld filler metal (filler passes) is also present, which is more pronounced for a joint with a soft root layer. Local strength mismatching is especially pronounced in the thickness direction of undermatched joints with homogeneous and heterogeneous welds, which has been determined by microhardness measurement (the distance between indents was 1 mm). The strength heterogeneity of the aforementioned welded joint is defined by the local mismatching factor ($M=R_{pweld}/R_{pbm}$). To evaluate the weld metal yield strength, the experimental equation ($R_p=3.15HV-168$) is often used, *[1]*, employing

microhardness measured values HV.1 in all joint points. In that manner, the strength mismatching factor M in every point of the welded joint is roughly determined.

The fracture toughness of homogeneous and heterogeneous undermatched weld joints was evaluated using standard static CTOD test (Figure 1). The testing temperature was -10ºC, in accordance with the recommendation of OMAE (Offshore Mechanics and Arctic Engineering) association. For CTOD testing, the single specimen method was used. To evaluate the fracture toughness of under-matched welded joints, standard, *[2-4]*, bending specimens (Bx2B, B = 36 mm) with deep (a/W=0.5) notches in the Heat-Affected Zone (HAZ) were used. For all specimens, fatigue pre-cracking was carried out with the GKSS Step-Wise High R ratio method (SHR) procedure. During the CTOD tests, the DC potential drop technique was used for monitoring the stable crack growth. The load line displacement (LLD) was also measured with the reference bar to minimize the effects of possible indentations of the rollers. The CTOD values were calculated in accordance with BS 5762, *[2]*, and also directly measured with a GKSS-developed δ_5 clip gauge, *[5]*, on the specimen's side surfaces at the fatigue crack tip over gage length of 5 mm.
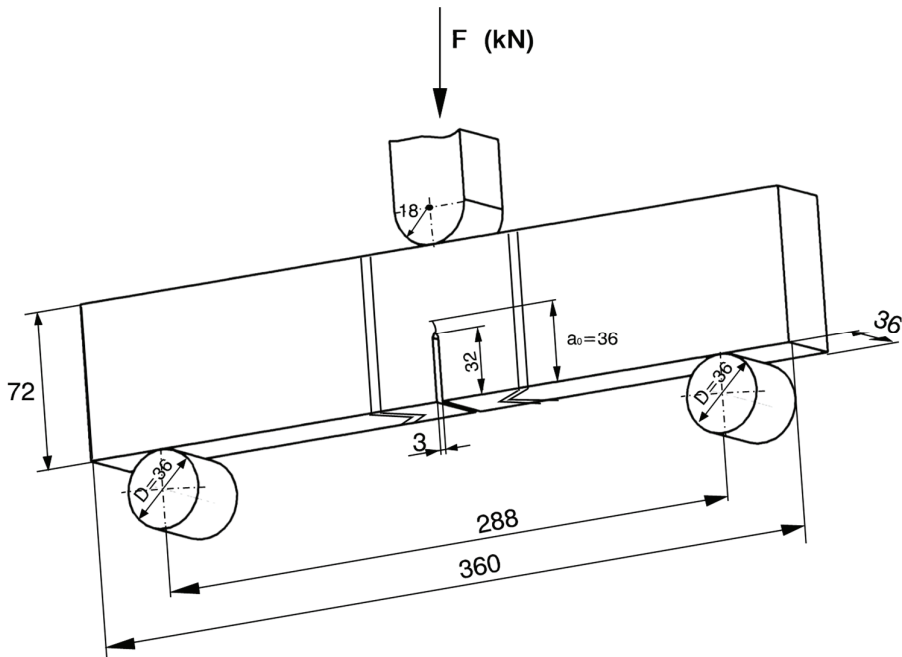

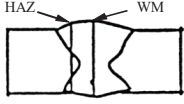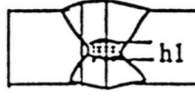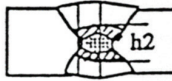**Figure 1:** *Shape and dimensions, and loading conditions for bend SENB specimens (B x 2B), made from homogeneous and heterogeneous undermatched weld joints*

For fracture mechanics, suitable standards for the treatment of welded joint- are not available yet, but different procedures exist, *[1, 6-8]*, that recommend different ways of fatigue crack positioning in weld joints. In light of this, different positions and depths (a/W) of fatigue cracks in homogeneous and heterogeneous welds were chosen, as shown in Table 1.

Table 1: *Fatigue crack positioning in SENB specimens (B x 2B) at weld joints*

SENB specimen	Specimen	Fatigue crack position	Crack depth a/W
Bx2B	M		0.5
	D		0.5
	E		0.5

3   RESULTS AND DISCUSSION

HAZ fracture toughness is relatively high, and in the case of homogeneous welds, it is much higher than the base material toughness (Figure 2). One reason for this was the composite fatigue crack front, including narrow HAZ regions with the Coarse Grain (CG) HAZ (Figure 3) of extremely low fracture toughness (Local Brittle Zones), but the remaining part, i.e., most of the fatigue crack front was contained, as were the more robust weld filler metal, base material, and remaining fine-grain HAZ (FG HAZ and Inter Critical (IC) HAZ).
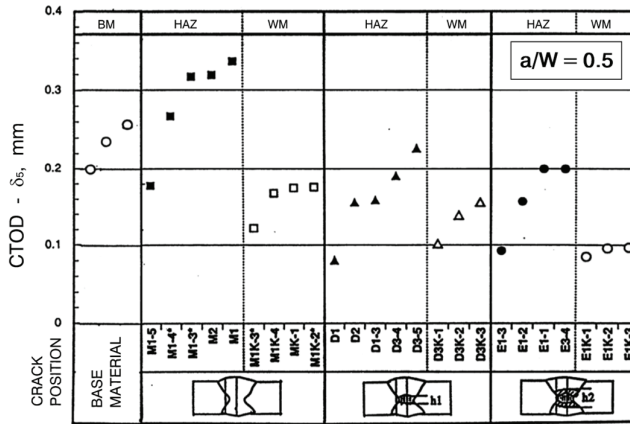
Figure 2: *CTOD (δ_5) fracture toughness values for specimens B x 2B in homogeneous and heterogeneous undermatched weld joints, measured at -10^0 C*

The main reason for this was different root welding heat input energy, causing different widths of HAZ in the root region of homogeneous and heterogeneous welds, consequently affecting the initiation of the final brittle fracture of the specimen. Specifically, the distance of fatigue crack tip front from the fusion line was approximately the same ($\approx$ 3.5 mm) for the CTOD specimens with the soft root layer and without it, [*1, 6-8]*.
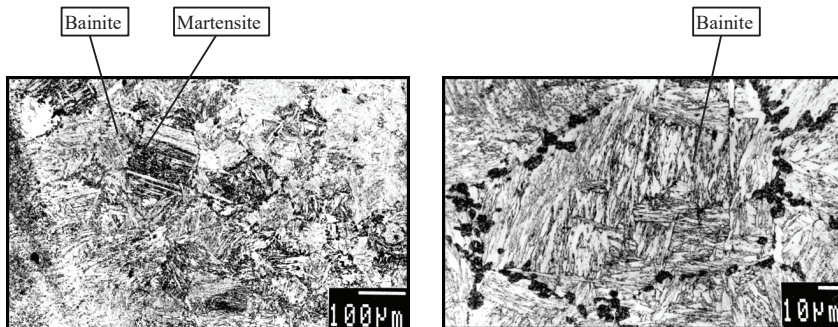

Figure 3: *CG HAZ with bainitic-martensitic microstructure, which was subsequently heated at a temperature between A_{c1} and A_{c3}, i.e., IC CG HAZ b) with distributed brittle M-A constituents along grain boundaries of primary grains (ASTM 4) with directed bainitic microstructure.*

The fatigue crack was sampled CG HAZ of two different widths related to CG HAZ region, which has influenced the value of HAZ fracture toughness of both welds (Figure 4). In CTOD specimens with cracks in HAZ of the homogeneous weld, brittle fracture initiation started in the weld material with the lowest value of mismatch factor M, because of the shielding effect of the overmatched root weld metal. The LBZs were already recorded during CTOD testing of welded joints as pop-ins. After that, an increase in stress intensification followed in HAZ, leading to the final brittle fracture of specimens through the CG HAZ and base material, which provided the least resistance in the specimen centre. The origin of final brittle fracture appeared in tougher

fine grain IC HAZ 8 (Figure 4). The crack path deviated to the softer base material, due to the shielding effect of the root overmatched weld metal.
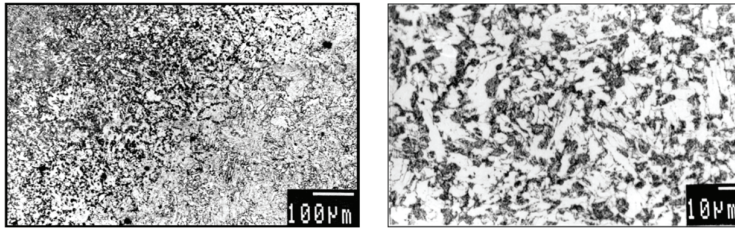

Figure 4: *HAZ, heated at intercritical temperature between A_{c1} in A_{c3} (IC HAZ). At higher magnification, the region of partial transformation to austenite, from which M-A constituents are formed, can be seen.*

In the case of CTOD testing of specimens with soft root layers, the first brittle fractures (LBZs) appeared in IC CG HAZ, which were recorded as small pop-ins. Due to high local strength mismatch between the base material and the soft root layer, the crack propagated towards the region of lower toughness, i.e., towards the fusion line and under-matched weld metal. The Fe_3C carbide was identified as the brittle fracture initiation point at the fracture surface using EDX analysis. The effect of the soft root layer on strain distribution along the fatigue crack front was so pronounced that it caused strain concentration in the soft root layer. Due to its low toughness, this initiated the final specimen fracture in coarse grain IC HAZ and crack path deviation towards the zone of the soft root layer, with a further reduction of toughness level, which would be achieved with higher soft root layer toughness.

The classification of CTOD resistance curves (Figure 5) for specimens with deep cracks in HAZ confirms the abovementioned analysis and conclusions that the HAZ fracture toughness of the homogeneous weld is much higher than the HAZ fracture toughness of the heterogeneous weld. By increasing the soft root layer thickness, the HAZ fracture toughness of the heterogeneous weld joint reduces and becomes lowest for the welded joint with the four-pass soft root layer (Figure 6), as is clear from the classification of CTOD resistance curves in Figure 5.

From the comparison of calculated (δ_{BS}) and measured (δ_5) CTOD values, a good agreement is evident, which is especially important for verifying detailed and directly measured CTOD - δ_5 values, for which one does not need to know the yield strength and the rotation factor as in the case of CTOD - δ_{BS} calculated values (Figure 7).
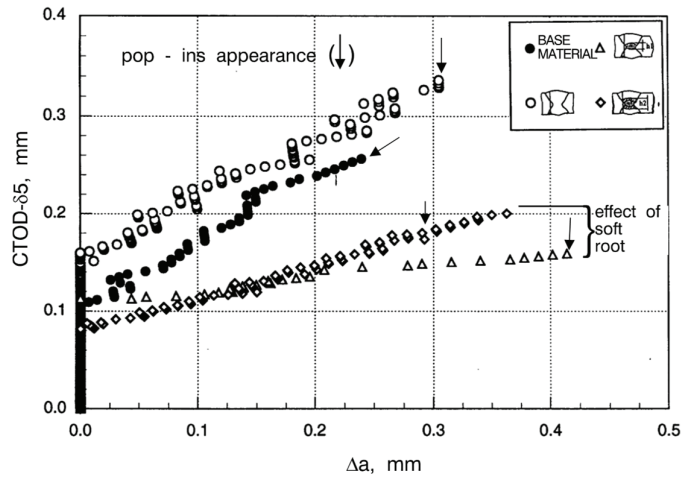
Figure 5: *Resistance curves for specimens (B x 2B) with deep crack (a/W = 0.5) in the HAZ of homogeneous and heterogeneous undermatched weld joints.*

This is essential in cases in which the fatigue crack tip front crosses regions with different strength levels and in which the effect of local strength mismatch at the crack tip is significant, as shown for fracture behaviour of undermatched joints with homogeneous and heterogeneous weld metal. More detailed analysis shows that CTOD-δ_5 values are generally lower than CTOD-δ_{BS} values, thus being more conservative.

As can be seen from Table 1, the fatigue crack was positioned in the HAZ and weld metal of homogeneous and heterogeneous undermatched weld joints. By positioning the fatigue crack in HAZ, a so-called "composite" fatigue crack front crosses the filler passes - HAZ - base material - HAZ - filler passes*. The distance between the fatigue crack front and the fusion line in the weld root region was approximately 3.5 mm in all specimens B x 2B (Figure 6 - Cross-section A-A). The primary aim of the fractographical investigation was to determine the location of brittle fracture initiation on the fracture surface of specimens B x 2B and to identify the brittle fracture initiation point by using Energy-Dispersive X-ray (EDX) analysis. Microstructures at the brittle fracture initiation point and around it, as well as the nature of the crack path deviation, were evaluated using the fracture surface cross-section through the brittle fracture initiation point. After the metallographic specimen was made, a detailed analysis of welded joint region at the crack tip and along the deviated crack path was done using an optical microscope and scanning electron microscope (SEM). In this manner, critical microstructures at the fatigue crack tip surroundings, where brittle fracture initiated, and microstructure, where it propagated and arrested later, were identified. For fractographical and metallographic analysis, the most representative fractures of specimens B x 2B were chosen, which also appeared in other specimens in an appropriate shape (Figure 6).
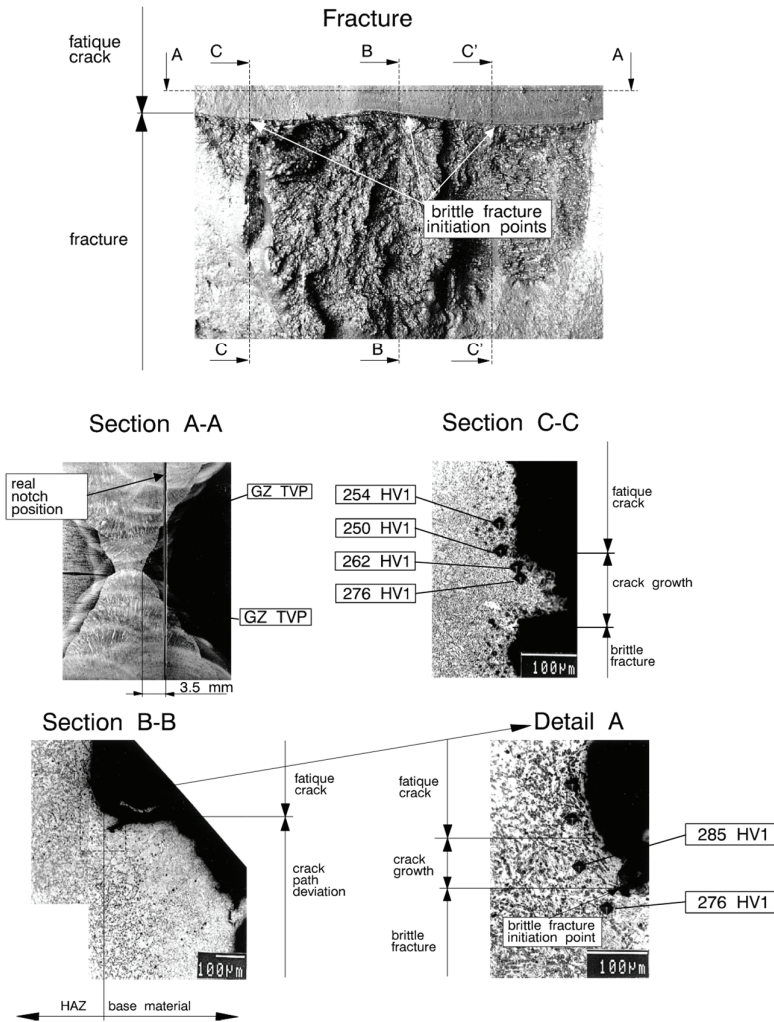
Figure 6: *Brittle fracture initiation points and crack path deviation on fractured specimen B x 2B with deep cracks in HAZ of* heterogeneous *undermatched weld joint*

Directly measured (δ_5) and calculated CTOD values (δ_{BS}) of fracture toughness for homogeneous and heterogeneous undermatched weld joints are summarized in Figure 7, for Single Edge Notch Bend (SENB) specimens, B x 2B. Different values of the rotational factor were used at the determination of calculated CTOD values (δ_{BS}) for surface cracks introduced in specimens in accordance with different a/W ratios. Rotational factor values r_p, [1], to determine the calculated CTOD - (δ_{BS}) were depended on crack depths (a/W) as follows:

for crack depths a/W = 0.25 - 0.37   » r_p = 0.25

for crack depths a/W = 0.43 - 0.48   » r_p = 0.44

Direct measurement (δ_5 method) and calculation (BS - 5762) of CTOD values from the measured Crack Mouth Opening Displacement (CMOD) values and estimation of δ values (δ_c, δ_u in δ_m) are described in *[1, 6-8]*. Evaluation of pop-in appearance using curves (F - CMOD, δ_5) is described in more detail in *[1]*. The CTOD testing was done at a temperature of -10° C.
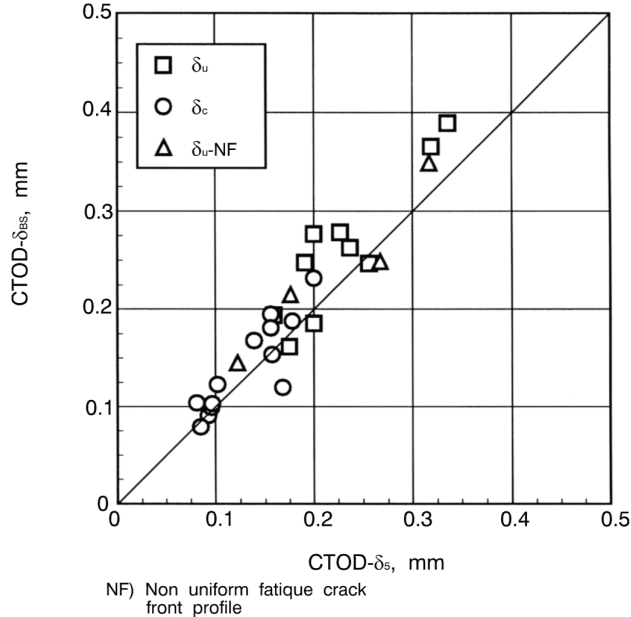

NF) Non uniform fatique crack front profile

Figure 7: *Comparison of directly measured (δ_5) and calculated (δ_{BS}) CTOD fracture toughness values of specimens B x 2B with deep crack (a/W = 0.5) in homogeneous and heterogeneous undermatched weld joints*

From Figure 7, it is clear that measured (δ_5) and calculated (δ_{BS}) CTOD fracture toughness values match approximately. More detailed analysis indicates that the direct measured method δ_5 gives more conservative CTOD values, *[1]*.

4   CONCLUSIONS

The fracture behaviour of specimens notched partly in the HAZ is strongly affected by microstructure at the crack tip. HAZ toughness improvement has been achieved due to its widening by higher input energy (Q + preheating) in the root region so that one part of the fatigue crack tip front passed through the normalized fine-grained HAZ region. The HAZ fracture toughness of heterogeneous welds is appreciably lower than the HAZ fracture toughness of homogeneous welds due to low ductility of the soft root layer, which has caused the brittle fracture initiation of welded joints by deviating the fracture path from HAZ to the soft root layer. Strength mismatch also has a significant influence on the real values of HAZ fracture toughness. The values obtained in both examples are not the real values for HAZ fracture toughness, because they were influenced by weld root strength properties. Fracture deviation towards the base material (homogeneous weld) overestimates HAZ fracture toughness, whereas fracture deviation towards the soft root layer (heterogeneous weld) underestimates it. Therefore, the

determination of HAZ fracture toughness is a complex problem that can be solved by synthetic multi-pass microstructures and their fracture toughness.

Good agreement between calculated (δ_{BS}) and measured (δ_5) CTOD values is evident from the comparison of CTOD results, verifying the method of direct measurement of CTOD, for which the material property data (e.g., yield strength) is not necessary, in contrast to the calculated CTOD values according to the standard BS 5762. This argument favours using direct measurement δ_5 at the crack tip in welded joints with local and global strength mismatching and precludes the application of standard BS 5762 for welded joints, which is valid for base material.

The brittle fracture initiation points of the root layer were indicated by EDX analysis as an Mn-Al-Si inclusion or TiCN carbide and they are found just below the blunting line, which is in agreement with the brittle fracture model theory. It should be noted that, for correct identification of a brittle fracture initiation point, it is of utmost importance to apply EDX analysis to both fracture surfaces. In the opposite case, it could happen that the EDX analysis detects some fictitious brittle fracture initiation point.

Acknowledgements

References

[1]   **Z. Praunseis:** *The influence of Strength Under-matched Weld Metal containing Heterogeneous Regions on Fracture Properties of HSLA Steel Weld Joint* (Dissertation in English). Faculty of Mechanical Engineering, University of Maribor, Slovenia, 1998

[2]   BS 5762, *Methods for crack opening displacement (COD) testing*, The British Standards Institution, London 1979.

[3]   ASTM E 1152-87, *Standard test method for determining J-R curves*, Annual Book of ASTM Standards, Vol. 03.01, American Society for Testing and Materials, Philadelphia, 1990.

[4]   ASTM E 1290-91, *Standard test method for crack-tip opening displacement* (CTOD) fracture toughness measurement, American Society for Testing and Materials, Philadelphia, 1991.

[5]   GKSS Forschungszentrum Geesthacht GMBH, *GKSS-Displacement Gauge Systems for Applications in Fracture Mechanic*.

[6]   **Z. Praunseis, M. Toyoda, T. Sundararajan**: *Fracture behaviours of fracture toughness testing specimens with metallurgical heterogeneity along crack front*. Steel res., Sep. 2000, 71, no 9,

[7]   **Z. Praunseis, T. Sundararajan, M. Toyoda, M. Ohata:** *The influence of soft root on fracture behaviors of high-strength, low-alloyed (HSLA) steel weldments*. Mater. manuf. process., 2001, vol. 16, 2

[8]   **T. Sundararajan, Z. Praunseis**: *The effect of nitrogen-ion implantation on the corrosion resistance of titanium in comparison with oxygen- and argon-ion implantations*. Mater. tehnol., 2004, vol. 38, no. 1/2

POWER LINE MAGNETIC FIELD DEVIATIONS FOR THREE DIFFERENT DEFINITIONS OF CURRENT UNBALANCE

ODSTOPANJE MAGNETNEGA POLJA DALJNOVODA ZA TRI RAZLIČNE DEFINICIJE TOKOVNEGA NERAVNOVESJA

Danka Antic [1,] Anamarija Juhas [2,] Miodrag Milutinov [3, ℜ]

Abstract

An estimation procedure of the public's exposure to the low-frequency magnetic field generated by overhead power lines, according to the international standards, implies measurement and an extrapolation. It is necessary to measure both the magnetic field around the lines and the current in the lines simultaneously. The extrapolation procedure implies the calculation of the maximum magnetic field that will occur when the line current achieves its maximum. The calculation relies on a proportion between the current in the power line and the magnetic field around the power line, which is valid only when the currents are balanced. Unfortunately, the standards do not cover the unbalanced cases. The relation between the current unbalance and magnetic field could improve the estimation procedure. In the literature, several different definitions of the current unbalance could be found. In this paper, a comparison of three different definitions of current unbalance and their relation to the deviation of a magnetic field are considered. The magnetic field is calculated in the vicinity of the bus bar. The same procedure could also be applied around overhead power lines. The definitions for the current unbalance used in this paper are derived from the existing definitions of the voltage unbalance. Only one of these three definitions considers phase unbalance. The relationships between current unbalance and the maximum deviation of the magnetic field are found to be proportional.

ℜ Corresponding author: Ph.D., Miodrag Milutinov, Tel.: +381 21 485 2577, Mailing address: Trg Dositeja Obradovica 2, 21000 Novi Sad, Serbia, E-mail address: miodragm@uns.ac.rs

[1,2,3] University of Novi Sad, Faculty of Technical Sciences, Trg Dositeja Obradovica 6, 21000 Novi Sad, Serbia

Povzetek

Po mednarodnih standardih se za izpostavljenost nizkofrekvenčnemu magnetnemu polju, ki ga ustvarjajo nadzemni daljnovodi opravljajo meritve, katere je potrebno ekstrapolirati. Meritve magnetnega polja okoli vodnika in toka v vodniku je potrebno opravljati v enakem časovnem intervalu. Postopek ekstrapolacije pomeni izračun največjega magnetnega polja, ki se pojavi pri največjem linijskem toku. Izračun temelji na razmerju med tokom v daljnovodu in magnetnim poljem okoli daljnovoda, kar velja le, če so tokovi v ravnovesju. Razmerje med tokovnim neravnovesjem in magnetnim poljem bi lahko izboljšalo postopek ocenjevanja, vendar standardi tega ne upoštevajo. V literaturi je moč zaslediti več različnih definicij tokovnega neravnovesja. V tem prispevku je predstavljena primerjava med tremi različnimi definicijami tokovnega neravnovesja in njihovega razmerja do odstopanja magnetnega polja. Magnetno polje se izračuna v bližini zbiralke, pri čemer se lahko enak postopek uporabi pri nadzemnih daljnovodih. Definicija tokovnega neravnovesja je v tem prispevku izpeljana iz napetostnega neravnovesja, pri čemer je ena od treh definicij izpeljana iz faznega neravnovesja. Ugotovitve so pokazale, da je razmerje med tokovnim neravnovesjem in največjim odstopanjem magnetnega polja sorazmerno.

1 INTRODUCTION

As reported in Bio-Initiative, *[1]*, electromagnetic pollution and its effects on various biological systems, both by short and continuous exposure, have been the subject of extensive research for several decades. The magnetic fields generated at 50/60 Hz by overhead power lines or bus bars inside the building are categorized as being extremely low frequency (ELF). The reference levels for general public exposure at the frequency of 50 Hz of the magnetic field and the magnetic flux density prescribed by ICNIRP, *[2]*, are 160 A/m and 200 µT, respectively. Reference levels for the occupational and public exposure to EMF, proposed by ICNIRP, *[2]*, became the basis for national legislation worldwide. Many countries have been adopted these levels without any changes. Serbia's national legislation, *[3]*, prescribes five times lower values; 32 A/m and 40 µT. The reference levels in the legislation are considerably lower and ensure additional safety for the general public.

Measurements of the magnetic field generated by overhead power line and estimation of the maximal exposure are covered by standards such as IEEE 644-1994 [4] and IEC 62110:2009, *[5]*. According to *[5]*, the values obtained by measurements are for the load conditions occurring at the time of measurement; therefore, these values need to be extrapolated to consider the maximum load of the circuits. This extrapolation procedure assumes that the power line currents are balanced, and equation (1) in *[5]* should be applied. The current unbalance causes the magnetic field deviation and thus introduces additional uncertainty in the adopted procedures, as authors have discussed in *[6]-[10]*. Multiple different definitions of the voltage unbalance could be found in the literature. As opposed to the previously published papers, *[6]-[10]*, in which only one of the definitions is used, in this research the authors utilized three definitions of current unbalance and consider the correlations of current unbalance with the deviation of the magnetic field for all three definitions.

2   CURRENT UNBALANCE

A three-phase circuit is considered balanced if the phase voltages and the phase currents are of the same amplitude and its phases are shifted by 2π/3 from each other. If either or both of these conditions are not met, the circuit is considered unbalanced (see e.g., *[11]*). Fig. 1 illustrated the phasor diagram of phase currents in balanced and unbalanced cases. Based on *[12]*, we adjusted three definitions of voltage unbalance for current unbalance. The first two definitions considered only amplitude unbalance, and the last one both amplitude and phase unbalance.
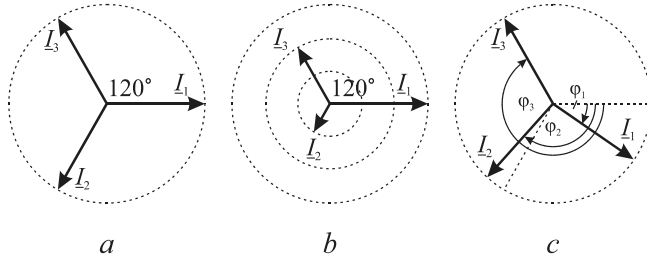

Figure 1: *Phasor diagrams of a) the balanced phase currents, b) magnitude unbalanced phase currents and c) phase unbalanced phase currents*

The first definition considers the maximum deviation of currents from the average value. It is defined by

$$u_{I1} = \frac{\max(|I_1 - I_{avg}|, |I_2 - I_{avg}|, |I_3 - I_{avg}|)}{I_{avg}} \cdot 100 \ \%, \qquad (2.1)$$

where I_1, I_2 and I_3, represent root-mean-square (RMS) values of the phase currents, while $I_{avg} = (I_1 + I_2 + I_3)/3$.

The second definition uses the difference of the maximum and the minimum RMS values as the measure for the unbalance. It is described by

$$u_{I2} = \frac{\max(I_1, I_2, I_3) - \min(I_1, I_2, I_3)}{I_{avg}} \cdot 100 \ \%. \qquad (2.2)$$

The third definition is the so-called " true definition of unbalance" because it accounts for both amplitude and phase unbalance. For $a = e^{j2\pi/3}$, it is given by:

$$u_{I3} = \frac{\left| \underline{I}_1 + a^2 \underline{I}_2 + a \underline{I}_3 \right|}{\left| \underline{I}_1 + a \underline{I}_2 + a^2 \underline{I}_3 \right|} \cdot 100 \ \%. \qquad (2.3)$$

All three current unbalances u_{I1}, u_{I2}, and u_{I3} are expressed in percentages.

3   CALCULATION METHOD

In this paper, the magnetic field is calculated near horizontally aligned bus bars illustrated in Fig. 2. The system consists of three phase conductors and a neutral one. The phase currents are denoted by I_1, I_2, and I_3. The current in the neutral conductor is denoted by I_N, where $\underline{I}_N = -\left(\underline{I}_1 + \underline{I}_2 + \underline{I}_3\right)$. Reference directions of the phase currents are out of the *xy* plane, and they are the same as the reference direction of the current in the neutral conductor. Conductors are assumed to be straight and parallel. Instead of the rectangular cross-section of the conductor, a current filament in the centre of the conductors are considered. The centre of the conductors is separated by $d = 15\,cm$. Applying the Biot-Savart law, the magnetic flux density is calculated in the cross-section of the bars (*xy* plane).
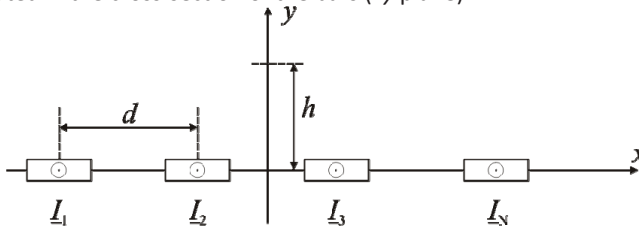

Figure 2: *Cross-section of the analysed system. Bus bars consisted of three phase and one neutral conductor horizontally aligned*

The deviation of magnetic flux density is defined as

$$\delta B = \frac{(B - B_0)}{B_0} \times 100\%, \tag{3.1}$$

where $B_0 = |\underline{B}_0|$ and $B = |\underline{B}|$ denote the magnetic flux density in balanced and unbalanced cases, respectively. B_0 is calculated assuming that the RMS values of all three phase currents I_1, I_2, and I_3 are the same and equal to the I_{avg}; and phases of the phase currents are 0, -120°, and 120°, respectively. Current unbalance is achieved either by changing the RMS value or the phase of the phase current. In what follows, the four cases of unbalance, listed in Table 1, are considered. The bold text is used to denote a quantity that sweeps its values through a defined range. The remain quantities keep their value unchanged.

Table 1: List of four analysed cases. The bolded quantity sweeps its values through a defined range

Case	RMS (A)	Angle (°)
1	a) $\boldsymbol{I_1}, I_2, I_3$ b) $I_1, \boldsymbol{I_2}, I_3$ c) $I_1, I_2, \boldsymbol{I_3}$	a), b), c) $\varphi_1, \varphi_2, \varphi_3$
2	a) $\boldsymbol{I_1}, \boldsymbol{I_2}, I_3$ b) $I_1, \boldsymbol{I_2}, \boldsymbol{I_3}$ c) $\boldsymbol{I_1}, I_2, \boldsymbol{I_3}$	a), b), c) $\varphi_1, \varphi_2, \varphi_3$
3	a), b), c) I_1, I_2, I_3	a) $\boldsymbol{\varphi_1}, \varphi_2, \varphi_3$ b) $\varphi_1, \boldsymbol{\varphi_2}, \varphi_3$ c) $\varphi_1, \varphi_2, \boldsymbol{\varphi_3}$
4	a), b), c) I_1, I_2, I_3	a) $\boldsymbol{\varphi_1}, \boldsymbol{\varphi_2}, \varphi_3$ b) $\boldsymbol{\varphi_1}, \varphi_2, \boldsymbol{\varphi_3}$ c) $\varphi_1, \boldsymbol{\varphi_2}, \boldsymbol{\varphi_3}$

For example, in the first case, the amplitude unbalance is obtained by sweeping the RMS of only one phase current in the range of 100 A ± 20 %. The currents in the other two phases are kept unchanged to the value of 100 A. In the second case, the amplitude unbalance is obtained by sweeping the RMS of two phase currents in the range of 100 A ± 20 %, while the value of the third phase current remains unchanged. In the third case, only the phase unbalance is allowed. The phase of only one phase current is changed in the range of $\varphi \pm 15°$. In the fourth case, the phases of two currents in the range of $\varphi \pm 15°$ being swept. In all considered cases, the RMS values of the currents take the values from 80 A to 120 A with the step size of 2 A, while the phases take the values from $\varphi - 15°$ to $\varphi + 15°$ with the step of $1°$.

Combinations of cases (1,3), (1,4), (2,3), and (2,4), in which both the amplitude and phase could be changed, are possible in practice, but they are not considered in this paper.

4   RESULTS

A deviation of magnetic flux density and current unbalance is calculated for all four cases at several points located on the *y*-axis at height h above the bus bar. Figures 3, 4, 5, and 6 show magnetic flux density relative deviation versus current unbalances at $h = 1\,m$. Each figure is related to one case, and each graph is related to one subcase. On all graphs, each set of dots is related to one of the definitions of current unbalance explained before. For the balanced currents $u_I = 0$, and the corresponding deviation is $\delta B = 0$. When the unbalance increases, the deviation also increases. The goals of this research are to determine the relation between these two quantities and to compare this relation for all three definitions.
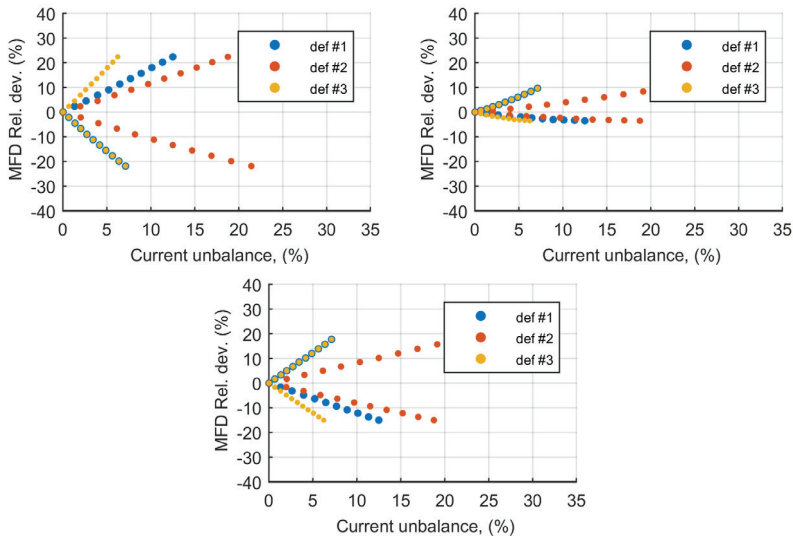
Figure 3: *Relation between current unbalance and deviation of the magnetic flux density for case 1, and subcase a, b and c, calculated at h=1m*
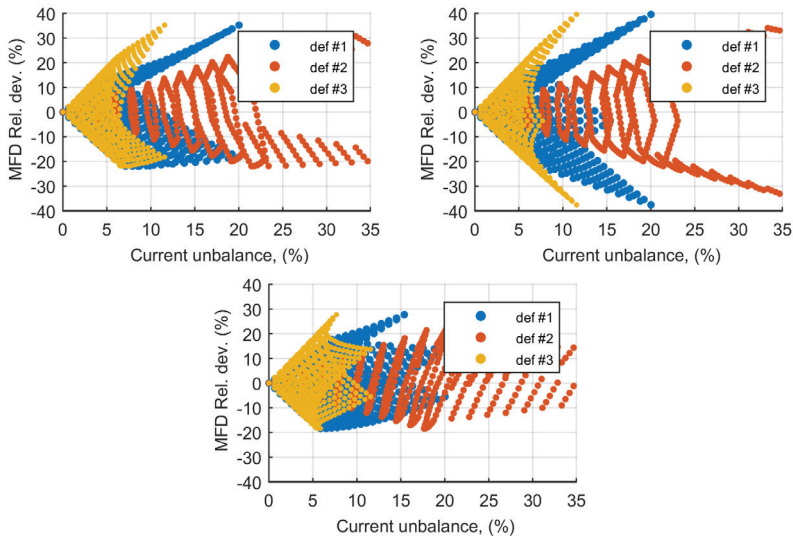

Figure 4: *Relation between current unbalance and deviation of the magnetic flux density for Case 2, and Subcases a, b and c, calculated at h=1m*
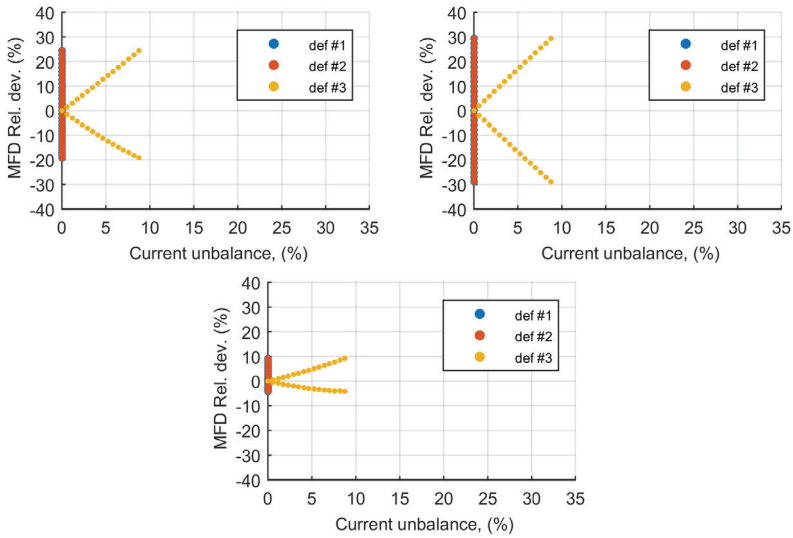
Figure 5: *Relation between current unbalance and deviation of the magnetic flux density for Case 3, and Subcases a, b and c, calculated at h=1m*
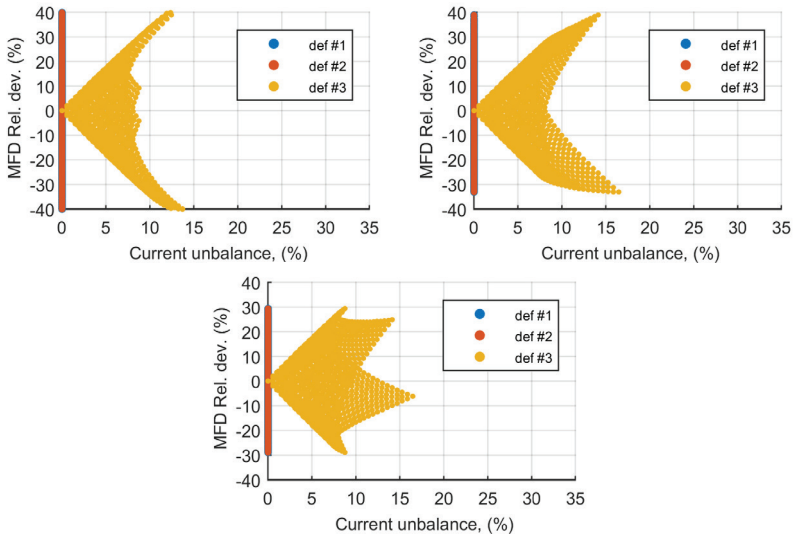

Figure 6: *Relation between current unbalance and deviation of the magnetic flux density for Case 4, and Subcases a, b and c, calculated at h=1m*

In Cases 1 and 2, an increase of the current unbalance results in an almost linear spreading of the range of magnetic field deviation, for all three definitions. In all graphs, δB populates the area bounded with a positive and a negative slope. This means that the relationship between current unbalance and the maximum magnetic field deviation can be described by:

$$\delta B = ku_I, \tag{4.1}$$

where k denotes the slope coefficient. Definition 3 experiences the fastest spreading and has the steepest slope. Recall that Definitions 1 and 2, do not consider the phase unbalance. Hence, in Cases 3 and 4, the current unbalance is nonzero only for Definition 3. In both cases, for Definition 3, a linear dependency between the current unbalance and the range of deviation can be observed.

In each case, subcase with the steepest slope, either positive or negative, can be determined. The slope coefficients for all previous graphs are listed in Table 2. The steepest slope achieved using Definition 1 has a coefficient $k = -3.38$, for Definition 2 the steepest slope has $k = 1.21$, while for Definition 3 $k = 3.63$. All these values are obtained in Case 2, Subcase c. By observing all three definitions, the steepest slope $k = 3.63$ is obtained by using Definition 3.

For example, the value of $k = 3.63$ shows that at 1 m above bus bars, the magnetic field generated by currents with 10% of unbalance is up to 36.3% higher than the magnetic field generated by balanced currents.

Table 2: Positive/negative slope coefficients for the point located on the y-axis at h=1m above bus bars.

Case	Subcase	Definition 1	Definition 2	Definition 3
1	a	1.79 / -3.38	1.19 / -1.13	3.57 / -3.38
	b	1.34 / -0.46	0.45 / -0.31	1.34 / -0.93
	c	2.47 / -1.22	0.82 / -0.81	2.47 / -2.44
2	a	2.47 / -3.38	1.19 / -1.13	3.61 / -3.48
	b	2.47 / -3.38	1.19 / -1.13	3.63 / -3.48
	c	2.47 / -3. 38	1.21 / -1.13	3.63 / -3.48
3	a	inf / inf	inf / inf	2.78 / -2.57
	b	inf / inf	inf / inf	3.38 / -3.38
	c	inf / inf	inf / inf	1.05 / -0.77
4	a	inf / inf	inf / inf	3.52 / -3.55
	b	inf / inf	inf / inf	3.52 / -3.55
	c	inf / inf	inf / inf	3.52 / -3.55

Increasing the distance from the bus bars from *h*=1m to *h*=2m another set of 12 graphs could be obtained. The steepest slope once again is obtained in Case 2 Subcase c, for Definition 3, with the correlation coefficient $k = 3.70$. Furthermore, at *h*=3m the correlation coefficient is $k = 3.71$. Hence, the correlation coefficient increases very slowly with the increasing the distance from the bus bars.
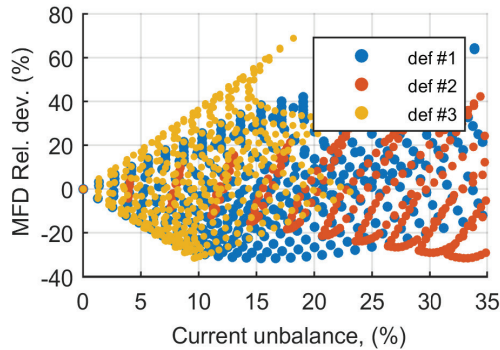
Figure 7: *Relation between current unbalance and deviation of the magnetic flux density for Case 2, and Subcase c, calculated at h=1m. I1=100A, while I2 and I3 are in a range from 60A to 140A*

Further increase of the current unbalance can be simulated by increasing the range of RMS values. Fig 7 shows the deviation of the magnetic flux density versus current unbalances in Case 2 Subcase c. RMS of the phase current I_2 and I_3 is in the range from 60 A to 140 A. The RMS value of the current I_1 remains 100 A. For Definition 3, the slope coefficient slightly increases from 3.63 to 3.78, implying that the upper boundary has a nearly constant slope.

5   CONCLUSIONS

The range of the magnetic field deviation considerably depends on the current unbalance. Moreover, the choice of the definition of the current unbalance significantly alters the corresponding range of magnetic field deviation. The widest range is obtained using the third definition, named "true definition of unbalance". For the analyzed configuration, the boundary of the range of the deviation for this definition has a slope of about 3.7, and a slight increase with increasing the distance from the bus bars. Also, the slope slightly increases with increasing the deviation of amplitudes of currents. It can be concluded that the relationship between current unbalance and the maximum deviation of the magnetic field is linear.

Acknowledgment

References

 [1]   BioInitiative Report*: A rationale for a biologically-based public exposure standard for electromagnetic fields (ELF and RF)*, http://www.bioinitiative.org

[2]   ICNIRP, *Guidelines for limiting exposure to time-varying electric and magnetic fields (1 Hz – 100 kHz)*, Health Physics, vol. 99(6), pp. 818-836, June 2010.

[3]   *Pravilnik o granicama izlaganja nejonizujućim zračenjima*, "Službeni glasnik RS", broj 104, 2009.

[4]   IEEE Std 644-1994, *Standard procedures for measurement of power frequency electric and magnetic fields from AC power lines*.

[5]   IEC 62110:2009, *Electric and magnetic field levels generated by AC power systems – Measurement procedures with regard to public exposure*.

[6]   **M. Milutinov, A. Juhas, N. Pekarić-Nađ,** *Analysis of effects of current unbalance on magnetic field*, 17th Int. Symp. Power Electronics – Ee 2013, Paper No. T.3.7, pp. 1-4, Novi Sad, Serbia, 30 Oct.-1. Nov., 2013.

[7]   **M. Milutinov, A. Juhas, N. Pekarić-Nađ**, *Magnetic field in vicinity of busbars with unbalanced currents*, 8th Int. PhD Seminar on Computational Electromagnetics and Electromag-netic Compatibility – CEMEMC 2014, Sep. 02-04, 2014, Timisoara, Romania.

[8]   **M. Milutinov, A. Juhas, N. Pekarić-Nađ**, *Relative deviation of magnetic flux density as a function of current unbalance*, 9th Int. PhD Seminar on Computational Electromagnetics and Bioeffects of Electromagnetic Fields - CEMBEF 2015, Niš, Serbia, Aug. 31, 2015, Proceedings of full papers, pp. 19-22.

[9]   **M. Milutinov, A. Juhas., N. Pekarić-Nađ**, *A study on exposure to magnetic field generated by unbalanced currents*, Trans. on Mathematics & Physics, Scientific Bulletin of Polytehnica, University of Timisoara, vol. 60(74), no.1, pp. 59-69, 2015.

[10]   **D. Antić, M. Milutinov, A. Juhas**, *Polarization of magnetic field in vicinity of busbars with unbalanced currents*, 10th Int. PhD Seminar on Computational Electromagnetics and Bioeffects of Electromagnetic Fields - CEMBEF 2017, Osijek, Croatia, Oct. 18, 2017, Proceedings of full papers, pp. 49-52

[11]   **J. Driesen, T. Van Craenenbroeck**, *Power Quality Applica-tion Guide: Voltage Disturbances - Introduction to Unbal-ance*, Copper Development Association, IEE Endorsed Pro-vide, May 2002

[12]   **T. H. Chen, C. H. Yang, N. C. Yang,** *Examination of the definitions of voltage unbalance*, Electrical Power and Energy Systems, vol. 49, 2013, pp. 380-385

Journal of Energy Technology

ASSESSMENT OF THE OPERATING CHARACTERISTICS OF BRUSHLESS DC MOTORS

OCENA DELOVNIH ZNAČILNOSTI BREZKRTAČNIH DC MOTORJEV

Vasilija Sarac[1,℞], Neven Trajchevski[2], Roman Golubovski[3]

Abstract

This paper presents the operating characteristics of brushless DC motors (BLDC) obtained via analytical, numerical, and simulation software, enabling steady-state and transient characteristics of a motor to be computed. Based on the catalogue data from the producer, Moog, a motor is simulated in a closed-loop control system fed by a voltage inverter. The accuracy of the derived models is verified by comparison with data from the producer. The developed analytical and simulation models enable the studying of various motor operating modes, such as no-load, rated load, and locked rotor, including motor starting characteristics. They are universal and can be easily applied to any brushless DC motor by simple replacement of the motor parameters. A numerical model in FEM software verifies the accuracy of previously derived models by obtaining the motor operating characteristics and the magnetic flux density distribution in a cross-section of the motor. The results obtained from all models have verified the proper design of the motor and laid out the path for further improvement with respect to the various motor parameters or operating characteristics.

℞ Corresponding author: Prof. Dr , Vasilija Sarac, Tel.: +389 32 550 650 , P.O. Box 201, 2000 Shtip, North Macedonia, E-mail address: vasilija.sarac@ugd.edu.mk

[1] University Goce Delcev, Faculty of Electrical Engineering, P.O. Box 201, 2000 Shtip, North Macedonia

[2] University Goce Delcev, Military Academy, Vasko Karangelevski bb, 1000 Skopje, North Macedonia

[3] University Ss. Cyril and Methodius, Faculty of Natural Sciences and Mathematics, Arhimedova bb, 1000 Skopje, North Macedonia

Povzetek

V tem prispevku so predstavljene delovne značilnosti brezkrtačnih DC motorjev (BLDC), pridobljene z analitično, numerično in simulacijsko programsko opremo, ki omogoča izračunavanje enakomernih in prehodnih značilnosti motorja. Na podlagi kataloških podatkov proizvajalca Moog je simuliran motor v krmilnem sistemu zaprtega kroga, ki ga napaja napetostni pretvornik. Natančnost izpeljanih modelov smo preverili s primerjavo s podatki proizvajalca. Razviti analitični in simulacijski modeli omogočajo preučevanje različnih načinov delovanja motorja, kot so brez obremenitve, nazivna obremenitev in zaklenjen rotor, vključno z značilnostmi zagona motorja. So univerzalni in jih je mogoče enostavno uporabiti na katerem koli brezkrtačnem DC motorju s preprosto zamenjavo parametrov motorja. Številčni model v programski opremi FEM preverja natančnost predhodno izpeljanih modelov z pridobivanjem delovnih lastnosti motorja in porazdelitvijo gostote magnetnega toka v prerezu motorja. Rezultati, dobljeni pri vseh modelih, so omogočili preverbo pravilne zasnove motorja, hkrati so podali pot za nadaljnje izboljšave glede na različne parametre motorja ali delovne lastnosti.

1   INTRODUCTION

In recent years, BLDC motors have gained popularity due to their wide application in robotics, automotive industrial equipment, and instrumentation. BLDC motors are similar in construction and operation to synchronous motors. Both BLDC and synchronous AC motors have permanent magnets (typically four or more) mounted on the rotor. The rotor magnets can be ferrite, which is less expensive but have a relatively low flux density, or rare-earth alloys, which have a higher flux density but often are more expensive. In BLDC motors, the stator coils are wound trapezoidally and the back-EMF produced has a trapezoidal waveform. Because of their trapezoidal waveform, direct current is required to obtain the best performance of BLDC motors. In contrast, synchronous AC motors are wound sinusoidally and produce a sinusoidal back EMF, so they require sinusoidal drive current to achieve their best performance. The development of power electronics has certainly contributed to the wide application of BLDC motors, as these types of motors are usually electronically commuted by the voltage inverter in closed-loop control systems, utilizing Hall effect sensors for sensing the motor position,*[1]-[2]*. However, sensorless techniques are also available for the detection of the motor position, and they are also widely used,*[3]-[4]*.Some of these sensorless schemes include a smoothing filter algorithm to improve the results obtained through an Extended Kalman Filter (EKF) algorithm in tracking the rotor position for sensorless control of brushless DC motors,*[5]*. Each motor modelling is highly dependent on the accurate identification of motor parameters. Often various optimization techniques are used for that purpose. In recent years, various controlling techniques have been investigated along with the simulation models that allow the accurate control and prediction of motor dynamic regimes,*[6]-[9]*, along with speed regulation techniques based on improved PI controllers utilizing particle swarm optimization algorithms, *[10]*. Torque ripple and the correlation with various commutation techniques are also investigated, *[11]*. Some authors focus on finding the most accurate analytical methodology for BLDC motor design, supported by various software,*[12]-[13]*. The procedure for the determination of optimal speed controller parameters of a PM brushless DC motor drive based on control quality indices is developed, and the impact of controller parameters on transient motor characteristics is presented in *[14]*. Other authors address the implementation of numerical techniques in modeling the various types of BLDC motors and present the properties and features of various magnetic parameters, *[15]-[17]*.

This paper covers various aspects of the BLDC motor design and operation, including motor analytical design and steady-state operating characteristics, motor dynamic analysis, when it is fed by the inverter, and finally motor numerical analysis in FEM software for obtaining various magnetic parameters and operating characteristics, giving an overall insight into complete motor design and operation. Firstly, a motor analytical model (AM) has been calculated in Ansys Maxwell software in order to identify motor parameters and operating characteristics. The accuracy of the developed analytical model was verified by comparing the obtained results from this model with available data from the motor producer, Moog,[18]. Once the analytical model was proved to be sufficiently accurate, the obtained motor parameters were used in the simulation model of a BLDC motor fed by an inverter, in a closed-loop system with Hall sensors, modelled in PSIM software. From this model, the transient characteristics of speed, torque, and motor current for rated load operating mode are obtained (PSIM model). Finite Element Analysis (FEA) is regularly used in the motor design as a necessary tool for estimating motor electromagnetic properties in terms of magnetic core saturation, losses, or even calculating various motor operating characteristics, [19]. The proper design of the motor should be based on good mechanical design regarding motor geometry accompanied by the adequate electrical design with respect to the winding parameters and properties of the electrical and the magnetic materials. In this paper, an analytical model of the motor including all design parameters, such as motor geometry, dimensions of the stator and rotor core, the geometry of the stator slots, and magnet poles, was derived on the basis of the very few parameters from the motor producer. Therefore, it was necessary that the obtained model of the motor be verified using FEA. From the FEA model, the magnetic flux density in the motor's cross-section was obtained, enabling estimation of the motor design in terms of the magnetic core saturation. From the last model, the motor torque and current were also calculated. The obtained results from AM, FEA, and the PSIM model were compared. They are useful in the assessment of the motor features in the various operating modes, allowing easy prediction of the motor operation during start up, at rated load, or no-load operation.

2   VARIOUS MODELS OF BLDC

2.1   Analytical model

The first step in defining the motor analytical model is to design the motor geometry properly. The design of the stator core, including the number and geometry of the slots, is done following the design procedure for asynchronous motors, [20]. Consequently, following the mentioned design procedure, presented in detail in [20], the stator core and the rotor dimensions are calculated. As this design procedure for calculating the analytical model of the motor is too long to be presented here, the motor cross-section calculated on the basis of this analytical procedure is presented in Fig. 1. Table 1 presents the key dimensions of the motor, calculated from the design procedure, which are used in the motor analytical model for calculating motor parameters and steady-state characteristics. Therefore, in the present paper, the analytical model of the motor is presented with the output results from this model, which are motor parameters, such as resistances and inductive reactances, presented in Table 2, as well as motor characteristics (torque, current, efficiency, speed, etc.) also presented in Table 2 for various operating regimes. The model is called the "analytical model" as it uses analytical formulas, presented in [20], for calculating motor cross-sections and the parameters of stator winding. Finally, as an output from this model, the motor steady-state characteristics of current, torque, efficiency and output power are calculated (Fig. 2, 3, 4, and 5). The outer motor dimensions like the outer diameter of the stator and the rotor as well as the number of the magnet poles are taken from the motor type BN42-53IP-03TFC of company Moog. Once all the dimensions of the motor are defined, including the properties of all materials, they are

input into the Maxwell software, on which basis the input model of the motor (obtained from analytical calculations) gives as an output the results presented in Table 2 and steady-state characteristics of the motor, presented in Fig. 2,3,4, and 5. Thus, the accuracy of this analytical model will be evaluated on the basis of its results presented in Table 2 and in Fig. 2,3,4, and 5, as these results cannot be obtained without an adequate model of the motor, obtained on the base of accurate analytical calculations of the motor dimensions and the winding parameters.

(a)	(b)
Motor cross-section	Stator slot
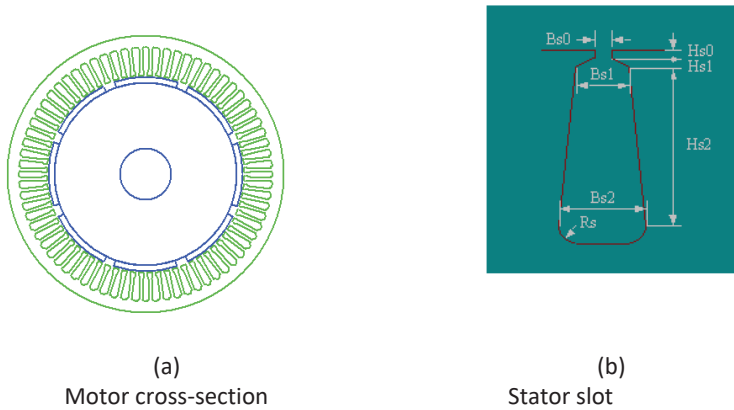
Figure 1: Motor layout

Table 1: Key dimensions of the motor

Stator	
Stator length (mm)	134.6
Outer diameter (mm)	155.14
Inner diameter (mm)	111.7
Nr. of slots	72
Stacking factor	0.95
Stator winding	
Winding layers	2
Parallel branches	1
Conductors per slot	8
Stator slot-dimensions (Fig. 1a)	
Hs0 (mm)	1
Hs1 (mm)	1.5
Hs2 (mm)	11.84
Bs0 (mm)	2
Bs1 (mm)	3.06
Bs2 (mm)	4.33
Rs (mm)	1
Rotor	
Outer diameter (mm)	109.1
Inner diameter (mm)	30
Length (mm)	134.6
Magnet thickness (mm)	3.2

As an output result, the analytical model, defined and solved in the Maxwell software, gives the motor parameters at rated load, no load, and locked rotor (Table 2).

Table 2: Parameters and operating characteristics of the analytical model

Steady-state parameters	
D-axis inductance (H)	0.00021
Q axis inductance (H)	0.00021
Zero-sequence inductance L_0 (H)	0.000084
Armature phase resistance at 20°C (Ω)	0.51
Rated load operation	
Armature current (A)	9.09
Input power (W)	1308
Output power (W)	879
Efficiency (%)	67.2
Rated speed (rpm)	2837
Rated torque (Nm)	2.96
Cogging torque (Nm)	0.956
Locked rotor operation	
Locked rotor torque (Nm)	17.14
Locked rotor current (A)	64.19

The analytical model was confirmed to be satisfactorily accurate by comparing the parameters and characteristics of the motor with the available data from the motor catalogue, *[18]*, (Table 3).

Table 3: Comparison between analytical model and producer

Parameter/characteristic	Analytical model	Motor producer
Peak torque (Nm)	17	17.14
Rated speed (rpm)	2820	2837
Rated torque (Nm)	2.959	2.958
Rated current (A)	9.1	10.20
Rated power (W)	879	874
Nr. of poles (/)	8	8
Armature phase resistance at 20°C (Ω)	0.51	0.408

According to Table 3, the analytical model is sufficiently accurate, and this model can be used further for deriving the steady-state operating characteristics, the simulation model for obtaining transient characteristics, and finally the numerical model for studying the magnetic flux density in the motor cross-section. The accuracy of the simulation model in PSIM software as well as the numerical model, based on FEM, are highly dependent on the accurate calculation of motor parameters (resistances and inductive reactances), the motor characteristics (current, power, etc.) and motor dimensions, all of which are obtained from the analytical model. From Fig. 2, 3, 4, and 5, for the rated speed of 2820 rpm, the rated current, torque, efficiency and output power of the motor can be read, and they are presented in Table 2. The presented steady-state

characteristics of the analytical model allow determining of the motor operation for various operating regimes. i.e., speeds.
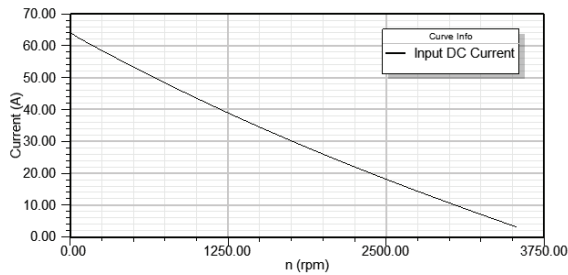

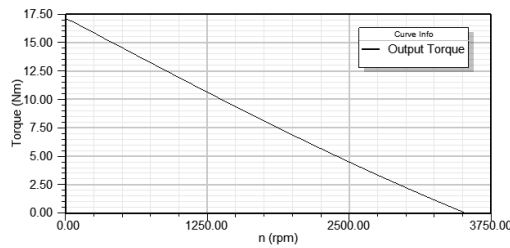***Figure 2:** Steady-state characteristic of the current*

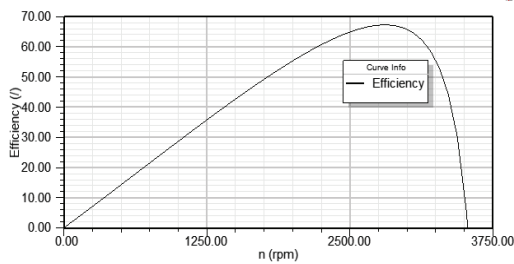***Figure 3:** Steady-state characteristic of the torque*

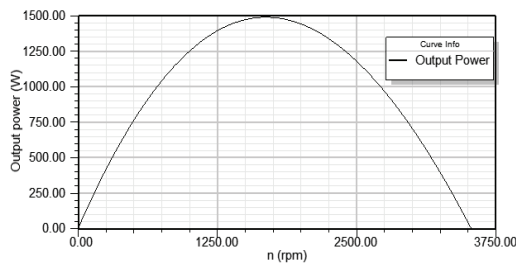***Figure 4:** Steady-state characteristic of the efficiency*

***Figure 5:** Steady-state characteristic of the output power*

During the continuous operations, the motor can be loaded up to the rated torque. The motor can run up to the maximum speed, which can be 1.5 times that of the rated speed, but the torque

starts to drop. Fig. 6 presents one typical torque-speed characteristic of the BLDC motor, *[21].* It contributes to the easier understanding of Fig. 3.
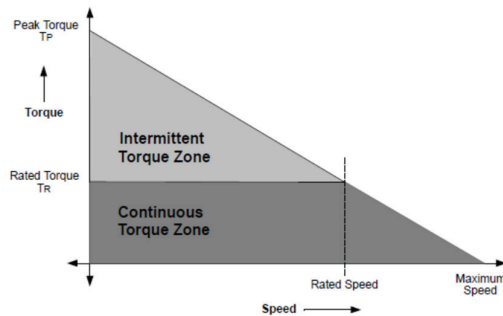
Figure 6: Typical torque/speed characteristic of BLDC motor, *[21]*

Applications that have frequent starts and stops and frequent reversals of rotation with the load on the motor require more than the rated torque. The motor can deliver a higher torque, maximum up to the peak torque, as long as it follows the speed torque curve. Output torque in brushless motors is proportional to stator current over the motor speed range. As for the efficiency factor, the expected maximum is around the rated speed. In practice, the efficiency factor is often lower due to the motor overheating, especially in high-speed applications.

2.2   PSIM model for modelling transient characteristics

Brushless DC motors use electronic switches for current commutation, allowing continuous rotation of the motor. These electronic switches can be connected in the H-bridge structure for single-phase motors or a three-phase structure for three-phase motors. Usually, the switches are controlled using pulse-width modulation (PWM), which converts the DC voltage into a modulated voltage, which easily and efficiently limits the startup current, control speed, and torque. The increase of the switching frequency increases the PWM losses while lowering the switching frequency limits the system bandwidth and can raise the ripple current pulses to the point that they become destructive or shut down the BLDC drive motor, *[22]*. The switching sequence is controlled so that it is synchronized with the position of the rotor. As a result, the stator produces a rotating magnetic field. The stator switches act like a commutator in classic DC motor. In brushless permanent magnet DC motors, the armature currents are commutated exactly according to the rotor position. The signal of the rotor position may be obtained from a position sensor, or from induced voltages for sensor-less control systems, *[23]*. Apart from the steady-state characteristics, motor-transient characteristics are an important part of motor analysis in terms of determining the motor acceleration time. As a six-pulse voltage inverter electronically commutates this type of motor, a closed-loop control scheme is simulated in Power PSIM software. This model will be referred to as a simulation model or PSIM model. BLDC commutation relies on feedback on the rotor position to decide when to energize the corresponding switches to generate the largest torque. The easiest way to accurately detect the position is to use a position sensor. In the simulation circuit, Hall sensors are used for sensing the motor position and the reference speed is set to the nominal speed of 2820 rpm. Fig. 7 presents the simulation circuit, while the output results of speed, torque, and current at rated load operation are presented in Figs 8, 9, and 10, respectively.
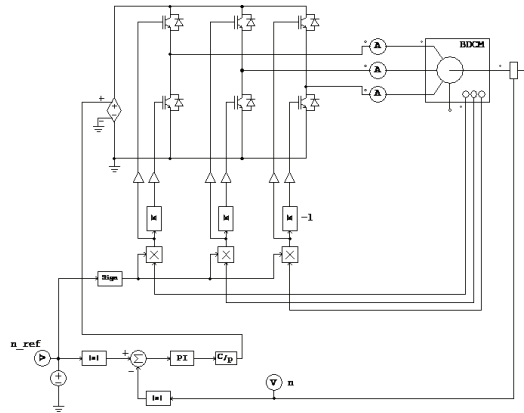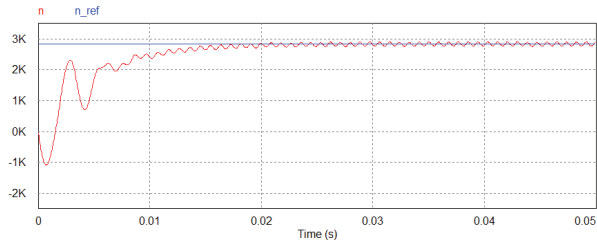
Figure 7: Simulation circuit in PSIM

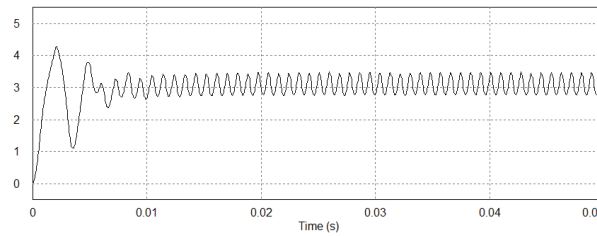**Figure 8:** Transient characteristic of speed

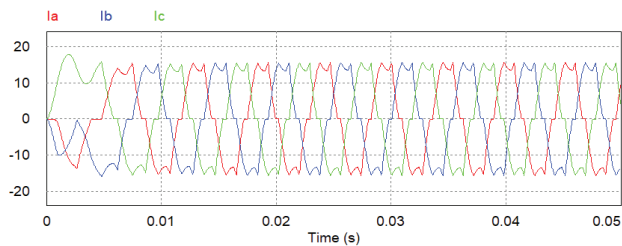**Figure 9:** Transient characteristic of torque

**Figure 10:** Transient characteristic of current

Motor accelerates up to the set speed for 0.02 s. After reaching the nominal speed, the motor current has an approximate rms value of 10 A, which is in good agreement with the results from the analytical model and motor producer data. A similar conclusion can be derived for the motor torque that reaches the average value of 3.3 Nm, which agrees very well with the producer data and the result from the analytical model.

2.3 Numerical FEM model

Recently, numerical modelling of electrical machines has gained popularity as a reliable and accurate tool in their design. This is due to the development of information technology that provides fast and accurate software capable of solving the complex differential equations that describe the machine's features. This is also the case with Maxwell's equations, which are solved by the aid of the finite element method in a relatively small region of the machine's cross-section, i.e., in each of the elements of the mesh, distributed all over the machine cross-section. Using Maxwell software, the motor is modelled in FEM, allowing the magnetic flux density distribution in the motor's cross-section to be computed. Fig. 11 presents the magnetic flux density distribution in a motor's cross-section at no-load, rated load, and locked rotor operation.
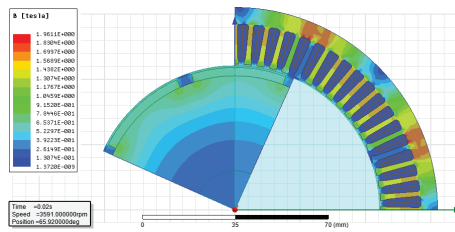
(a) no-load operation
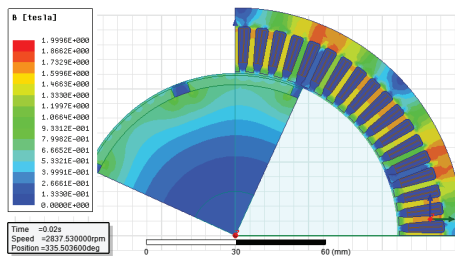
(b) rated load operation
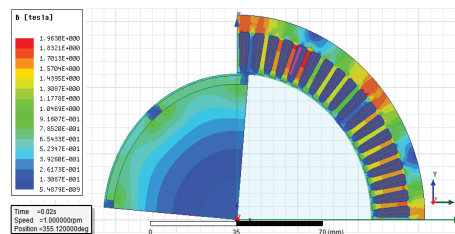
(c) locked rotor operation

Figure 11: Flux density distribution

3   DISCUSSION OF RESULTS

The main objective of this research is to establish a satisfactorily accurate analytical model of the BLDC that will serve as a basis for the further modifications and the improvements of the motor design. The results from the analytical model that include motor parameters and operating characteristics are presented in Table 2 and Figs. 2, 3, 4, and 5. A comprehensive analysis has been carried out, which includes the simulation model for obtaining the transient characteristics of the motor, the numerical model of the motor for verification of the motor design, and the available data from the producer of the motor. A comparison of the results from all the models of the motor verifies the accuracy of the models and establishes the starting model of the motor, subject to further modifications and optimization. By comparing the results from the simulation and the numerical model, it can be concluded that computed current in the motor's numerical model (Fig. 12) follows the shape of the characteristics and the rms value of the current, computed using the simulation model in PSIM (Fig. 10). A similar conclusion can be derived for the torque characteristics as torque reaches the average value of around 3.1 Nm in the numerical model, which is very close to the data from the motor producer, simulation, and analytical model of the motor (Fig. 9). Starting torque from the analytical model is adequate with data from the producer and starting torque calculated from the numerical model. Table 4 presents the comparison of the obtained results from all models of the motor with the data of the motor producer.

Table 4: *Comparison between analytical model and producer*

Parameter/characteristic	AM	PSIM model	NM	Motor producer
Peak torque (Nm)	17	/	18.2	17.14
Rated speed (rpm)	2820	2837	2837	2837
Rated torque (Nm)	2.959	3.3	3.15	2.958
Rated current (A)	9.1	10.6	10.1	10.20
Rated power (W)	879	/	/	874
Resistance (Ω)	0.51	0.51	0.51	0.408

By comparing the obtained results of motor torque, current, and output power from the analytical model of the motor (Table 3 and Figs. 2, 3, 4, and 5) at the rated speed, with the obtained results from motor simulation model (Figs 8, 9 and 10) and the obtained results of motor current and torque from the numerical model (Fig. 12 and 13), it can be concluded that the results from all three models of the motor are close one to another, which verifies the accuracy of the analytical model of the motor as a good starting point for further modifications and optimizations of the analysed motor.

4   CONCLUSION

The main objective of this paper is to derive various computer models of a brushless DC motor, capable of computing motor parameters and operating characteristics, useful for the assessment of motor operation in various operating regimes. Starting from very sparse catalogue data, the analytical model, set for computer modelling, was derived. The analysis was extended with the simulation model for determining motor-transient characteristics. The third motor model is the numerical model that allows the computing of magnetic flux density in the motor cross-section, as well as motor torque and currents during starting and rated load operation. The obtained results from all motor models are compared, showing very good alignment with data from the motor producer. The derived models are useful for the inexpensive and reliable replacement of motor testing in laboratories in order to determine the motor features and behaviour in various operating modes. Furthermore, the derived models are universal. They can be easily applied to any brushless DC motor by simple replacement of motor parameters. Establishing the accurate model of the BLDC motor is a good basis for the further modification of the motor design aiming towards the optimization of parameters that impact motor efficiency and its overall operation.

References

[1]   **M. Hiaojun, W. Guodong, L. Chunguang, Y. Huaibin**:*The electric drive system for brushless DC motor*, 2014 IEEE Conference and Expo Transportation Electrification Asia-Pacific, p.p. 1-3, 2014

[2]   **B. Tibor, V.Fedak, F. Durovsky:***Modeling and simulation of the BLDC motor in MATLAB GUI*, IEEE International Symposium on Industrial Electronics, Poland, p.p. 1403-1407, 2011

[3]   **J. C. Gamazo-Real, E. Vázquez-Sánchez, J. Gómez-Gil:***Position and speed control of brushless DC motors using sensorless technique and application trends*, Sensors, Vol.10, Iss. 7, pp. 6901-6947, 2010

[4]   **M.B. Astik, P. Bhatt, B.R. Bhalja:** *Analysis of sensorless control of brushless DC motor using unknown input observer with different gains*, Journal of Electrical Engineering, Vol.68,   Iss.2, pp. 99-108, 2017

[5]   **S. S. Alex, A.E. Daniel:** *An efficient Position Tracking Smoothing Algorithm for Sensorless Operation of Brushless DC Motor Drives*, Modelling and Simulation in Engineering, Vol. 2018, p.p. 1-9, 2018

[6]   **C. Ogbuka, C. Nwosu, M. Agu:***A fast hysteresis current-controlled permanent magnet synchronous motor drive based on field orientation*, Journal of Electrical Engineering, Vol.67,   Iss.2, p.p. 69-77, 2016

[7]   **I.V. Abramov, Y. R. Nikitin, A.I. Abramov, E.V. Sosnovich, B. Božek:***Control and diagnostic model of brushless DC motor*, Journal of Electrical Engineering, Vol. 65, Iss. 5, p.p. 277-282, 2014

[8]   **M.R. Hazari, E. Jahan, Md. E. Siraj, Md. T. I. Khan, A.M. Saleque:***Design of Brushless DC (BLDC) motor controller*, 2014 International Conference on Electrical Engineering and Information & Communication Technology, p.p. 1-5, 2014

[9]   **R. Arulmozhiyal, R. Kandiban:** *An intelligent speed controller for Brushless DC motor*, 7th IEEE Conference on Industrial Electronics and Applications, Singapore, p.p. 16-21, 2012

[10]   **W. Xie, I-S. Wang, H-B. Wang:** *PI Controller of Speed Regulation of Brushless DC Motor Based on Particle Swarm Optimization Algorithm with Improved Inertia Weights*, Mathematical Problems in Engineering, Vol. 2019, p.p. 1-12, 2019

[11]   **Y. Ji, B. Li, J. Sun:** *Harmonic Analysis on Torque Ripple of Brushless DC MotorBased on Advanced Commutation Control,* Journal of Control Science and Engineering,   Vol. 2018, p.p. 1-9, 2018

[12]   **C. He, T. Wu:** *Permanent Magnet Brushless DC Motor and Mechanical Structure Design for the Electrical Impact Wrench System*, Energies, Vol.11, Iss. 6, p.p 1-24, 2018

[13]   **C. Carunaiselvane:** *Generalized Procedure for BLDC Motor Design and Substantiation in MagNet 7.1.1 Software*, International Conference on Computing, Electronics and Electrical Technologies,Nagercoil, India,p.p. 18-25, 2012

[14]   **P. Crnošija, R. Krishnan, T. Bjažić:** *Transient Performance Based Design Optimization of PM Brushless DC Motor Drive Speed Controller*, IEEE International Symposium of Industrial Electronics, Dubrovnik, Croatia, p.p. 881-886, 2005

[15]   **H. M. C. Beigi:** Design*Optimization and FEM Analysis of a Surface-Mounted Permanent-magnet Brushless DC Motor,* International Journal of Engineering Transactions B: Applications, Vol. 31, Iss. 2, p.p. 339-345, 2018

[16]   **P. Srinivas:** *Design and FE Analysis of BLDC Motor for Electro-Mechanical Actuator*, Journal of Electrical Systems, Vol. 11. Iss. 1, p.p. 76-88, 2015

[17]   **C.C. Hwang, P.L. Li, C.T.Liu, C. Chen:** *Design and analysis of a brushless DC motor for applications in robotics*, IET Electric Power Applications, Vol.6, Iss. 7, p.p. 385-389, 2012

[18]   **Moog: Inc:** *Motion Technology Catalog*, rev. 4, 2018

[19]   **D-C. Popa, B. Vărăticeanu, D. Fodorean, P. Minsiunescu, C. Martis:** *High Speed Induction Motor in electric vehicles*,*Electrotehnica, Electronica, Automatica (EEA)*, Vol. 64, Iss. 3,p.p. 5-11,2016

[20]   **I. Boldea, S.A. Nassar:** *The induction machines design handbook*, CRC Press,Boca Raton, USA, 2010

[21]   **P. Yedamale:** *Brushless DC (BLDC) Motor Fundamentals*, Microchip Technology Inc, AN885, 2003

[22]   **Y. Zhao, Y. Yu:** *Brushless DC motor Fundamentals Application Note*, MPS, AN047, Rev. 1.0, 2014

[23]   **Ansys INC:** *Maxwell On line Help*, Release 18.0, December 2016

MAIN TITLE OF THE PAPER
SLOVENIAN TITLE

*Author[1], Author [2], Corresponding author*ℜ

Keywords: (Up to 10 keywords)

Abstract

Abstract should be up to 500 words long, with no pictures, photos, equations, tables, only text.

Povzetek

(Abstract in Slovenian language)

<u>Submission of Manuscripts:</u> All manuscripts must be submitted in English by e-mail to the editorial office at jet@um.si to ensure fast processing. Instructions for authors are also available online at http://www.fe.um.si/en/jet/author-instructions.html.

<u>Preparation of manuscripts</u>: Manuscripts must be typed in English in prescribed journal form (MS Word editor). A MS Word template is available at the Journal Home page.

A title page consists of the main title in the English and Slovenian language; the author(s) name(s) as well as the address, affiliation, E-mail address, telephone and fax numbers of author(s). Corresponding author must be indicated.

<u>Main title</u>: should be centred and written with capital letters (ARIAL bold 18 pt), in first paragraph in English language, in second paragraph in Slovenian language.

<u>Key words</u>: A list of 3 up to 6 key words is essential for indexing purposes. (CALIBRI 10pt)

<u>Abstract</u>: Abstract should be up to 500 words long, with no pictures, photos, equations, tables, - text only.

<u>Povzetek</u>: - Abstract in Slovenian language.

<u>Main text</u> should be structured logically in chapters, sections and sub-sections. Type of letters is Calibri, 10pt, full justified.

ℜ Corresponding author: Title, Name and Surname, Organisation, Department, Address, Tel.: +XXX x xxx xxx, E-mail address: x.x@xxx.xx

[1] Organisation, Department, Address

[2] Organisation, Department, Address

Chapter examples:

1   MAIN CHAPTER

(Arial bold, 12pt, after paragraph 6pt space)

1.1   Section
(Arial bold, 11pt, after paragraph 6pt space)

1.1.1 Sub-section

(Arial bold, 10pt, after paragraph 6pt space)

Example of Equation (lined 2 cm from left margin, equation number in normal brackets (section. equation number), lined right margin, paragraph space 6pt before in after line):

Equation   (1.1)

Tables should have a legend that includes the title of the table at the top of the table. Each table should be cited in the text.

Table legend example:

Table 1: *Name of the table (centred, on top of the table)*

Figures and images should be labelled sequentially numbered (Arabic numbers) and cited in the text – Fig.1 or Figure 1. The legend should be below the image, picture, photo or drawing.

Figure legend example:

Figure 1: Name of the figure (centred, on bottom of figure, photo, or drawing)

References

[1]   **N. Surname:** *Title,* Journal Title, Vol., Iss., p.p., Year of Publication

[2]   **N. Surname:** *Title,* Publisher, Year of Publication

[3]   **N. Surname:** *Title* [online], Publisher or Journal Title, Vol., Iss., p.p., Year of Publication. Available: website (date accessed)

Examples:

[1]   **J. Usenik**: *Mathematical model of the power supply system control*, Journal of Energy Technology, Vol. 2, Iss. 3, p.p. 29 – 46, 2009

[2]   **J. J. DiStefano, A.R. Stubberud, I. J. Williams**: *Theory and Problems of Feedback and Control Systems*, McGraw-Hill Book Company, 1987

[3]   **T. Žagar, L. Kegel:** *Preparation of National programme for SF and RW management taking into account the possible future evolution of ERDO* [online], Journal of Energy Technology, Vol. 9, Iss. 1, p.p. 39 – 50, 2016. Available: http://www.fe.um.si/images/jet /Volume 9_Issue1/03-JET_marec_2016-PREPARATION_OF_NATIONAL.pdf (7. 10. 2016)

Example of reference-1 citation: In text *[1],* text continue.

Nomenclature

(Symbols)	(Symbol meaning)
t	time

JET